Design Aspects of Inductive Power Transfer Systems for Electric Vehicle Charging

DANIEL PEHRMAN

Department of Electrical Engineering
Division of Electric Power Engineering
CHALMERS UNIVERSITY OF TECHNOLOGY
Gothenburg, Sweden 2019

Design Aspects of Inductive Power Transfer Systems for Electric Vehicle Charging
DANIEL PEHRMAN

Design Aspects of Inductive Power Transfer Systems for Electric Vehicle Charging
DANIEL PEHRMAN
Department of Electrical Engineering
Chalmers University of Technology

Abstract

During the last decade the transition towards electric propelled vehicles has had an upswing and electric vehicle (EV) sales has increased steadily. This is much due to legislations on lowering emissions but also due to lower total cost of ownership. Eliminating tailpipe emissions is a major driver for the electrification of the transportation sector. In order to meet the goals on CO_2-emissions the shift towards EVs in the transportation sector needs to increase even faster. Two of the holdbacks for a more widespread penetration of EVs are the limited range and the frequent and slow recharging compared with internal combustion engine (ICE) vehicles. With technology advancements in energy storage and power electronics the energy storage and charging of EVs could instead become a strength for EVs.

An emerging technology for recharging EVs is by inductive power transfer (IPT). Having no contact between the vehicle and the charger makes it inherently safe with respect to electrical shocks. Furthermore, with no moving parts the maintenance requirement becomes minimal. This technology is especially appealing in automated charging applications and opportunity charging. Charging can be initiated automatically for buses at bus stops, delivery trucks when loading or unloading goods, taxis at taxi ranks and at traffic light intersections. By charging more frequently the life time of the battery is increased. Alternatively, a smaller battery pack can be used. IPT can also be integrated seamlessly in public parking places without obscuring the view and without any risk of getting unplugged.

The fundamental principle of IPT is based on power transfer by non-radiative electro-magnetic fields. Challenges with designing IPT systems involve trade-offs between efficiency, misalignment tolerance, gravimetric- and area related power density, and stray fields. In this thesis a thorough analysis of coil design is presented and the most common compensation topologies are evaluated. Two series-series compensated IPT chargers are designed and prototypes are developed and verified experimentally. Firstly, a home charger rated for 3.7 kW input power with an air gap of 210 mm is designed. The coil design is based on analytical results in

combination with the finite element method. In this system, the current in the primary coil is constant, regardless of alignment and coupling between coils. At rated load with aligned coils, 94 % dc-to-dc efficiency is achieved. The second charger is a fast charger rated for 50 kW with an air gap of 180 mm. The dc-to-dc efficiency is above 95 %, down to 10 % of the rated load, including losses in the full-bridge inverter, transmitting- and receiving coil with compensation, and the output rectifier.

By using SiC MOSFETs a high switching frequency (85 kHz) for power transfer and a more compact coil design can be utilized. The area related power density of the vehicle assemblies of the two chargers are 20 kW/m^2 and 148 kW/m^2 respectively. A limiting factor for the maximum achievable power transfer capability is the stray fields around and inside the vehicle. A simulation model of the stray field is developed and verified with measurements. With the home charger mounted on a plug-in hybrid electric vehicle (PHEV), measurements show that the magnetic flux density is less than 10 % of the allowed emission limits at the most severe locations.

Index Terms: inductive power transfer, electric vehicle charging, coupled inductors, series-series compensation, series-parallel compensation, finite element method (FEM), silicon carbide (SiC), full-bridge resonant inverter, stray field measurements, shielding

Acknowledgements

Daniel Pehrman
Gothenburg, Sweden
Spring, 2019

List of Acronyms

ac	Alternating Current
BP	Bipolar
CO_2	Carbon Dioxide
dc	Direct Current
DD	Double-D
DDQ	Double-D Quadrature
EV	Electric Vehicle
FEM	Finite Element Method
FoM	Figure-of-Merit
GA	Ground Assembly
HEV	Hybrid Electric Vehicle
ICE	Internal Combustion Engine
I-PFC	Interleaved Power Factor Correction
IPT	Inductive Power Transfer
MOSFET	Metal Oxide Semiconductor Field Effect Transistor
NP	Non-Polarized
P	Polarized
PHEV	Plug-in Hybrid Electric Vehicle
SiC	Silicon Carbide

SoC	State of Charge
THD	Total Harmonic Distortion
VA	Vehicle Assembly

List of Symbols

δ — Skin depth

ψ_{ii} — Flux linkage of coil

λ — Wavelength

ψ_{ij} — Flux linkage

ρ_i — Radius of current loop i in cylindrical coordinates

ρ_P — Radial coordinate of point P

ρ_{cu} — Resistivity copper

μ — Permeability ($\mu_0 \mu_r$)

ω — Angular frequency

σ — Conductivity

a — Radius of coil

b — Winding width

$\boldsymbol{B}$ — Magnetic flux density vector

c — Speed of light in vacuum

C_{oss} — Output capacitance of MOSFET

d — Duty cycle

$\boldsymbol{D}$ — Electric displacement vector

d_s — Strand diameter

d_w — Wire diameter

$\boldsymbol{E}$	Electric field vector
$E(m)$	Complete elliptical integral of second kind $(m = k^2)$
$F(m)$	Complete elliptical integral of first kind $(m = k^2)$
$\boldsymbol{H}$	Magnetic field intensity vector
i_1	Primary side current
i_2	Secondary side current
I_{sc}	Short-circuit current
$\boldsymbol{J}$	Current density vector
k_B^2	Elliptical modulus for magnetic flux density
k_L^2	Elliptical modulus for self-inductance
k_M^2	Elliptical modulus for mutual inductance
k	Coupling factor between coils
L	Geometric mean of self-inductances
L_i	Self-inductance of coil
$L_{\sigma i}$	Leakage inductance coil
L_a	Cantilever model leakage inductance
L_b	Cantilever model magnetizing inductance
L_m	Magnetizing inductance
M	Mutual inductance between coils
n	Turns ratio of coils
n_s	Number of strands in litz wire
N	Number of turns in coil
N_e	Turns ratio of coils with respect to coupling factor
Q	Geometric mean of quality factors
Q_i	Native quality factor
$Q_{i,L}$	Loaded quality factor
r	Series resistance of coil

r_w	Wire radius
R_L	Load resistance
R_{load}	Linearized load resistance
S_c	Maximum apparent power of compensated coils
S_u	Maximum apparent power of uncompensated coils
T_p	Time of switching period
V_1	Primary side voltage
V_2	Secondary side voltage
V_{dc}	Inverter dc-link voltage
V_{oc}	Open-circuit voltage
x_P	x-coordinate of point P
y_P	y-coordinate of point P
z	Air gap
z_P	z-coordinate of point P

Contents

Appendices **73**

1. Introduction

1.1 Background and Motivation

During the past decades electric propulsion has become the most promising technology for the vehicle market to move away from the internal combustion engine (ICE) running on fossil based fuel. Starting with hybrid electric vehicles (HEV) that could benefit from regenerative breaking and thus lowering the emissions, to plug-in hybrid vehicles (PHEV) that allowed zero emission propulsion. During the latest decade the pure electric vehicles (EV), which propels solely on electric power, has also had a big breakthrough. The main motivator behind the electrification of vehicles is legislation on lowering emissions. This has led to technical developments from manufacturers in electrification which, together with subventions, has made EVs and PHEVs an attractive choice for customers.

Passenger vehicles propelled by an ICE typically refuels gasoline with a flow rate of 40 - 50 L/min [1]. The energy density of gasoline is 9.61 kWh/L [2] which corresponds to an average of 432 kWh/min or equivalently 26 MW. This can be compared to today's fast charging stations, which can supply up to 350 kW [3] i.e. approximately 1 % of the refueling power of ICE vehicles. Even when taking into account the higher efficiency of EVs, it is still less than an order of magnitude lower in terms of traveling distance per time spent charging. The longer recharging time combined with the high cost and low energy density of batteries are the two main limitations that prevent a larger market penetration of EVs.

In [4] the utilization of vehicles in free-floating car sharing services was studied for different cities. The utilization rate was on average between 4.0 % - 21.6% of the time (58 - 306 minutes per day) and driven for an average distance

between 5 km - 27 km. With an energy consumption for commercial EVs ranging from 117 - 268 Wh/km [5] the needed energy to recharge during the non-using time for the most utilized case is 7.2 kWh (27 km and 268 Wh/km). This would allow a vehicle to be recharged in less than 2 hours with a 3.7 kW charger. The utilization rate (when the vehicle is either driven or charged) would still be less than 30 %.

EVs will, most likely, not be competitive with ICE vehicles in terms of time-to-charge. A solution to make EVs more attractive than ICE vehicles would be to eliminate any user interactivity when it comes to recharging the vehicle. One promising solution of achieving this is by the means of inductive power transfer (IPT). IPT eliminates any physical contact between the charger and the vehicle and charging can be initiated automatically. Since there is no physical contact it also reduces the risk of electric shocks which makes it much safer than conductive charging. It can also be implemented to charge while driving, so called dynamic charging, as well as for bi-directional power transfer. Caravans of EVs can distribute energy between them or EVs can be used as an uninterruptible power supply (UPS) for the house or support for the grid.

Connecting a cable from the mains to the on-board charger in the vehicle is, as of today, the main approach when recharging EVs. The power level of plug-in chargers are usually up to 22 kVA (three-phase, 32 A) or 43 kVA (three-phase, 63 A), yet far from all manufacturers provides an on-board charger that can handle these power levels. Instead of supplying the on-board charger with AC the battery can be charged directly from a DC-source and bypassing the on-board charger, which allows for even higher charging power. DC-charging is mainly utilized for fast charging with power levels ranging from 50 kW up to 350 kW and is realized by converting the mains voltage to DC externally of the vehicle.

Except for the time-to-charge, the differences between refueling and recharging in terms of human interaction are next to nothing. Solutions to automate the refueling and recharging process with robotic systems have been proposed [6, 7]. The most successful implementations of automatic conductive recharging has been for buses in public transportation [8] where the charging is initiated automatically on some of the stops along the route or at the end stations. There are also pilot projects where conductive charging has been installed in the road or with overhead lines and pantographs and vehicles are powered while driving [9, 10].

Although conductive charging is a feasible solution for charging EVs there are several drawbacks. The procedure of plugging is inconvenient and if the

2

purpose of parking is not to recharge, plugging in is often forgotten or ignored. Also, having a lot of charging stations in public spaces is visually unaesthetic. There is also both a trip risk or obstruction and risk of electrical hazard with plugged in EVs. With IPT, charging stations can be integrated seamlessly and non-obstructively. Lastly, the risk of sabotage is reduced significantly with IPT. A combination of DC charging for extremely high power charging (>500 kW) at dedicated fast charging stations, and IPT for home-, opportunity- and on-road charging could be the most cost effective, safe and convenient solution for charging EVs.

1.2 Inductive Power Transfer State-of-the-Art

With the development in switching devices, IPT has gained a substantial amount of attention lately and can potentially be the next technology for charging EVs. Standards for IPT in EV charging applications have been proposed and initially four power levels have been established, shown in Table 1.1.

Table 1.1: Power levels of IPT charging

Level	Power
1	3.7 kVA
2	7.7 kVA
3	11 kVA
4	22 kVA

A prominent figure-of-merit (FoM) for IPT system is the product kQ, where k is the coupling factor and Q is the geometric mean of the quality factors of the coils. For a fixed operating frequency, load, and coil alignment, the FoM is determined solely by the coil design, making the coil design crucial for designing high efficient IPT systems. One of the most popular approaches is by using a planar coil design due to the misalignment tolerance, ease of mounting and flat design. Several planar coil topologies for high power IPT have been proposed in recent research [11–14]. The planar coil topologies can be divided into two categories; polarized or non-polarized, where the former has distinct magnetic poles while the later has one pole on either side of the coil and the return path of the magnetic field surrounds the coil. Illustrations of different planar coil topologies are shown in Fig. 1.1a-Fig. 1.1e and a non-planar coil topology (solenoid) is shown in Fig. 1.1f.

It is indicated whether the coil topology is polarized (P), non-polarized (NP) or if it can be operated in either way (P/NP).

In the literature, several studies and comparisons of the different coil topologies has been conducted [15–17]. In general, the non-polarized topologies shows better performance when the coils are perfectly aligned and the polarized topologies are better in misaligned condition. Some of the most prominent IPT systems are listed in Tab. 1.2. The key parameters and what type of coils used are indicated.

Table 1.2: Summary of wireless charging systems

| Organisation	Power	Air gap	Frequency	Efficiency	Coil topology
Witricity [18]	11 kW	210 mm	85 kHz	94%	N/A
ORNL [19]	120 kW	150 mm	22 kHz	97%	P
KAIST[1][20]	100 kW	260 mm	20 kHz	81.7%	P/NP
ETH [21]	50 kW	170 mm	85 kHz	95%	NP
UOA [22]	3.5 kW	132 mm	85 kHz	91.4 %	P
Plugless [23]	7.2 kW	100 mm	N/A	N/A	N/A

[1] dynamic charging

One of the obstacles for IPT to have a breakthrough in EV charging is the lack of standardization. As of today, SAE international has recommended practices for wireless charging of light-duty and plug-in EVs. The recommended practices are aimed for stationary vehicle charging and cover requirements on power levels, frequency band, efficiency, electromagnetic compatibility and safety [24]. Similar recommended practices for dynamic charging are likely to come in the near future.

The principle of IPT is by using a high frequency magnetic field for power transfer. Since the separation between the coils is large, the leakage inductance and stray fields are high. The International Commission on Non-Ionizing Radiation Protection (ICNIRP) are investigating the effects of electric and magnetic fields (EMF) exposure for humans. Based on this, guidelines for the low-frequency range and up to 10 MHz are formulated [25]. The most recent guidelines are from 2010 which replaced the previous guidelines from 1998. In the latest guidelines, the exposure limits were increased for magnetic fields and more strict for electric fields. The limits for magnetic flux density and electric field regarding both occupational and public exposure for different frequencies are plotted in Fig. 1.2a and Fig. 1.2b
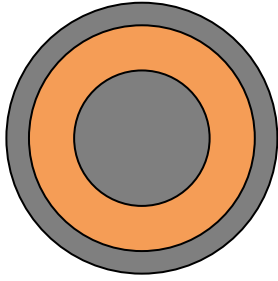
(a) Circular coil, (NP)
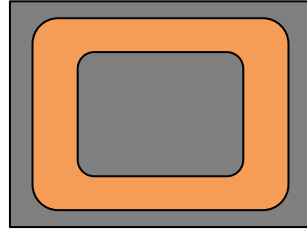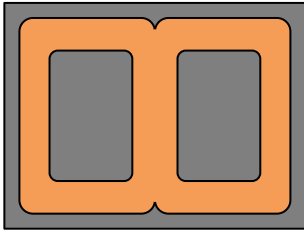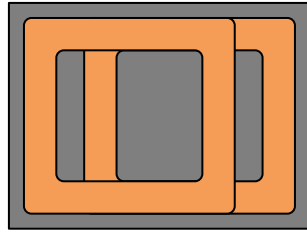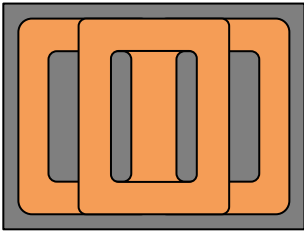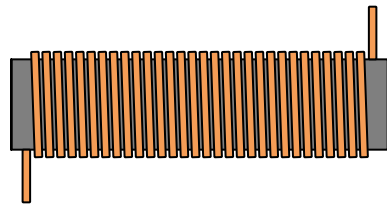
(b) Rectangular coil, (NP)

(c) double-D (DD) coil, (P)

(d) Bipolar (BP) coil, (P)

(e) Double-D Quadrature (DDQ) coil, (P/NP)

(f) Solenoid, (P)

Figure 1.1: Planar coil topologies; polarized (P), non-polarized (NP) or operated as either (P/NP)

respectively. With complex geometries the magnetic field is difficult to determine analytically. Instead, finite element method (FEM) simulations can be used, although FEM simulations are computational demanding for detailed models. A common approach for designing coils is based on equally sized coils with radii four times the air gap, which gives a ball park solution. The design is then iterated by FEM simulations to obtain a feasible design. However, with this approach the design space becomes large and the computational effort becomes high. With an analytical approach the design space can be narrowed down, reducing the computational demand.
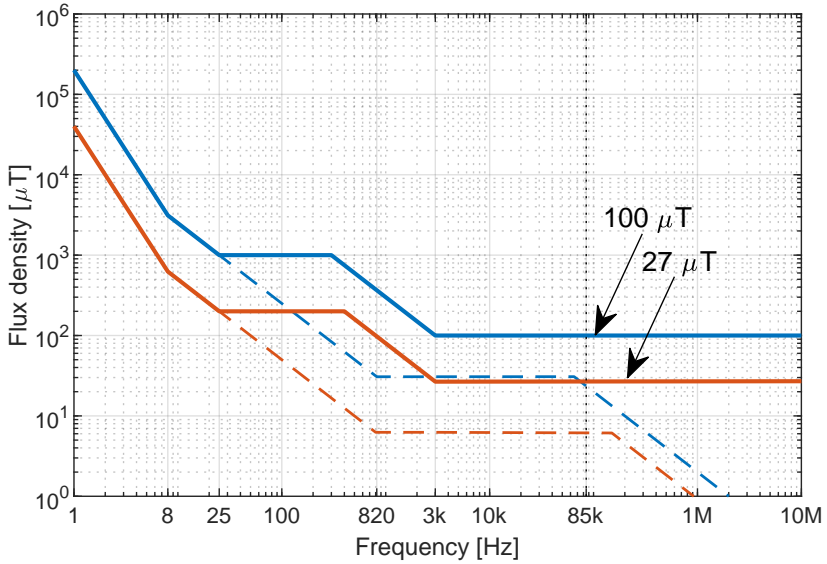
Furthermore, the reactive power from the leakage fields needs to be supplied by the power electronics which leads to additional losses. A solution to this is to connect reactive power compensation in forms of capacitors to compensate for this. In early research of IPT single sided compensation was utilized [26, 27]. The single sided compensation can only fully compensate for the reactive power in a single operating point. In more recent research double-sided compensation topologies has been proven superior regarding flexibility, efficiency and power transfer capability [28–31]. If more complex compensation topologies are used, such as LCC or LCL, more flexibility and controllability can be achieved. Although, with more components the system becomes more complex and the efficiency is reduced.

1.3 Purpose of the Thesis and Main Contributions

With the above mentioned critical topics on IPT, this thesis aims to analyze sizing, operation and stray fields of IPT in static EV charging applications. The theoretical results are verified with experimental tests. A thorough analysis of inductive power transfer is presented and based on the analysis, two prototypes are developed and tested. The main contributions of the work are identified as follows:

- A maximum current control method is proposed and its functionality is proven. The method is based on a constant current supplying the primary coil, regardless of alignment. This method gives a robust control and eliminates the need for a dc/dc converter on the primary side.

- A novel design approach that combines analytical equations and finite element method to determine the optimal coil size for a fixed air gap is suggested.

(a) Magnetic flux density limits
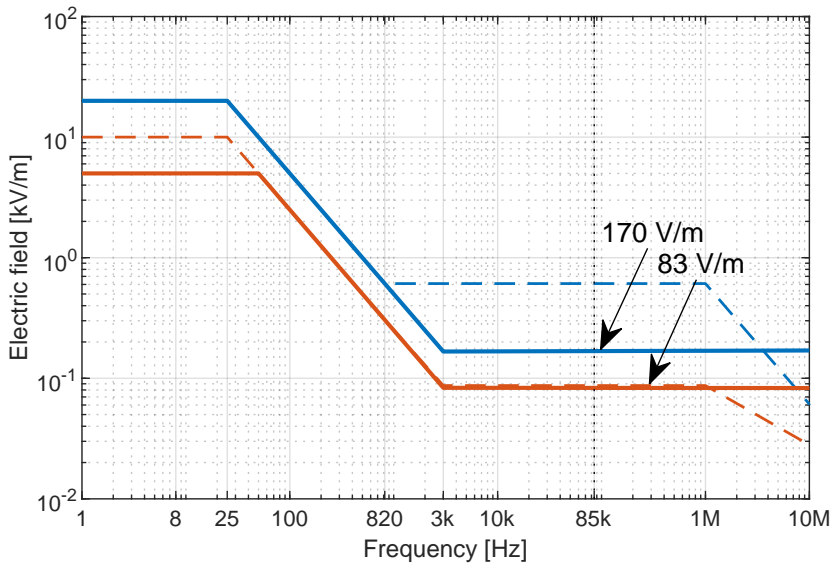
(b) Electric field limits

Figure 1.2: Magnetic flux density and electric field limits for occupational (blue) and public (orange) exposure from ICNIRP 2010 (solid) and ICNIRP 1998 (dashed).

With an analytical approach as a starting point, the computational effort is significantly reduced. This method results in a higher coupling factor than same sized coils, especially for large air gap-to-coil ratios.

- The magnetic stray field from a charger mounted on a vehicle is investigated and quantified. A simplified simulation model is developed and simulation results are experimentally verified. It is shown that the designed charger easily fulfills the stray field emission limit.

- A back-to-back setup without any additional dc/dc converters is proposed for high power testing. With the back-to-back setup, the power supply only needs to provide the losses. Without extra dc/dc converters on the input and output, the system complexity is reduced and efficiency measurements on a system level are easier and more accurate.

1.4 Thesis Outline

The thesis is divided into three parts. Firstly, Chapter 2 and Chapter 3 focuses on the analysis and modeling of coupled coils and compensation topologies for IPT. Secondly, in Chapter 4 and Chapter 5 the design aspects together with simulations and experimental results of two prototypes are presented. Lastly, in Chapter 6 the thesis is concluded and future work is proposed.

1.5 List of Publications

I D. Pehrman and Y. Liu, "Design and Stray Field Evaluation of Inductive Power Transfer in Electric Vehicle Charging," 2019 Fourteenth International Conference on Ecological Vehicles and Renewable Energies (EVER) , Monte-Carlo, Monaco, 2019.

II A. Kersten, Y. Liu, D. Pehrman and T.Thiringer, "Rotor Design of Line-Start Synchronous Reluctance Machine with Round Bars," in IEEE Transactions on Industry Applications, 2019.

III A. Kersten, Y. Liu and D. Pehrman, "Rotor Design of a Line-Start Synchronous Reluctance Machine with Respect to Induction Machine for Industrial Applications," 2018 XIII International Conference on Electrical Machines (ICEM), Alexandroupoli, 2018, pp. 393-399.

IV Y. Liu, D. Pehrman, O. Lykartsis, J. Tang and T. Liu, "High frequency exciter
    of electrically excited synchronous motors for vehicle applications," 2016 XXII
    International Conference on Electrical Machines (ICEM), Lausanne, 2016, pp.
    378-383.

 V D. Pehrman, Y. Liu, Y. V. Serdyuk and P. Karlsson, "Study on filtering
    performance of soft magnetic composite inductors for switching harmonics
    in 3-phase 70 kW PWM converter systems," 2015 IEEE Energy Conversion
    Congress and Exposition (ECCE), Montreal, QC, 2015, pp. 3024-3031.

CHAPTER 1.

2. Modeling and Design of Loosely Coupled Coils

The design of the coils is the most crucial aspect regarding efficiency, leakage fields and misalignment tolerance for IPT. For IPT in EV charging applications the space on the receiving side is limited which entails that the secondary coil needs to be relatively small while the ground clearance of the vehicle, and thus the air gap, is large. In this chapter the modeling and design of coils with a high ratio of air gap to coil radii are analyzed.

2.1 Coupled Inductor Modeling

If the wavelength of the current is long in comparison with the length of the coil ($\lambda >> l_{coil}$), the coils can be modeled as a lumped parameter model. The wavelength is approximately

$$\lambda \approx \frac{c}{f} \tag{2.1}$$

where c is the speed of light and f is the frequency. As shown in Tab. 1.2 the operating frequency for high power IPT is typically in the order of $10^4 - 10^5$ Hz, which corresponds to a wavelength in the range of $\lambda \sim 3 - 30$ km, and the length of the coil wire is usually well below 100 m, which motivates the use of lumped parameters in the analysis. The lumped model approximation is in general not valid for IPT applications where the frequency is above the MHz range or for long coil tracks, e.g. in dynamic charging.

Assuming two coils with N_1 and N_2 turns in the vicinity of each other, as

shown in Fig 2.1. If a current I_1 flows in the first coil it creates a magnetic field
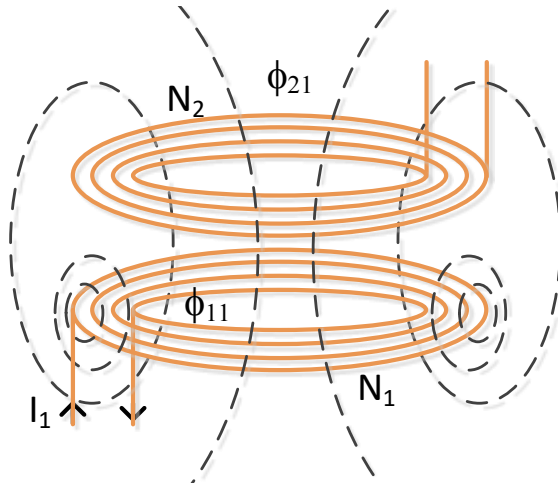
Figure 2.1: The current I_1 produces a magnetic flux ϕ_{11} of which ϕ_{21} couples with a secondary coil

proportional to the current flowing in the coil according to Ampere's law,

$$\nabla \times \boldsymbol{H} = \frac{\partial \boldsymbol{D}}{\partial t} + \boldsymbol{J} \tag{2.2}$$

where $\boldsymbol{H}$ is the magnetic field intensity vector, $\boldsymbol{D}$ is the electric displacement vector and $\boldsymbol{J}$ is the current density vector. If the current I_1 is alternating it generates an alternating magnetic field. The amount of the magnetic field that passes through the area enclosed by the secondary coil (denoted ϕ_{21} in Fig. 2.1) will give rise to an EMF in the secondary coil according to Faraday's law,

$$\nabla \times \boldsymbol{E} = -\frac{\partial \boldsymbol{B}}{\partial t} \tag{2.3}$$

where $\boldsymbol{E}$ is the electric field and $\boldsymbol{B}$ is the magnetic flux density which are related to the current density $\boldsymbol{J}$ and magnetic field intensity $\boldsymbol{H}$ as

$$\begin{aligned} \boldsymbol{E} &= \frac{\boldsymbol{J}}{\sigma} \\ \boldsymbol{H} &= \frac{\boldsymbol{B}}{\mu} \end{aligned} \tag{2.4}$$

where σ is the conductivity and $\mu = \mu_0 \mu_r$ is the permeability of the medium. The polarity of the induced voltage in (2.3) will be such that the induced voltage yields a current that opposes the change in the magnetic field that induced it.

The mutual inductance of two coils is defined as the magnetic flux generated by the primary coil that penetrates the area enclosed by the secondary coil and can be written

$$M = \frac{\phi_{21}}{I_1} \tag{2.5}$$

where M is the mutual inductance, ϕ_{21} is the linked flux generated in the primary coil due to I_1 that penetrates the area enclosed by the secondary coil. From this, the time domain voltage equations for two coupled coils become

$$\begin{aligned} v_1(t) &= L_1 \frac{\partial i_1(t)}{\partial t} + M \frac{\partial i_2(t)}{\partial t} \\ v_2(t) &= M \frac{\partial i_1(t)}{\partial t} + L_2 \frac{\partial i_2(t)}{\partial t} \end{aligned} \tag{2.6}$$

where L_1 and L_2 is the primary- and secondary self-inductance respectively. The coupling factor, k, is defined as the part of flux that is linked between the coils divided by the total flux

$$k = \frac{M}{\sqrt{L_1 L_2}}. \tag{2.7}$$

Another important parameter of the coil is the quality factor, Q, which is the ratio of reactive and active power. For an unloaded coil the quality factor is

$$Q = \frac{VAr}{P} \tag{2.8}$$

$$= \frac{\omega L}{r} \tag{2.9}$$

where ω is the frequency, L is the self-inductance and r is the resistance accounting for losses in the coil. Equation (2.8) is also valid for loaded coils where VAr is the reactive power and P is the sum of the power consumed by the load and the losses in the coil.

2.1.1 Transformer Model

Coupled inductors can be modeled by the traditional transformer model, illustrated in Fig. 2.2, with either one or two leakage inductances. These models are commonly used for iron core transformers, although there are some major differences between iron core transformers and coupled inductors. In an iron core transformer the leakage inductance is very small and can often be neglected. For IPT the coils are weakly coupled and the leakage inductance can be up to ten times bigger than the magnetizing inductance. This means that there is more energy stored in the magnetic field for loosely coupled coils.

(a) Two leakage inductance model   (b) Cantilever transformer model
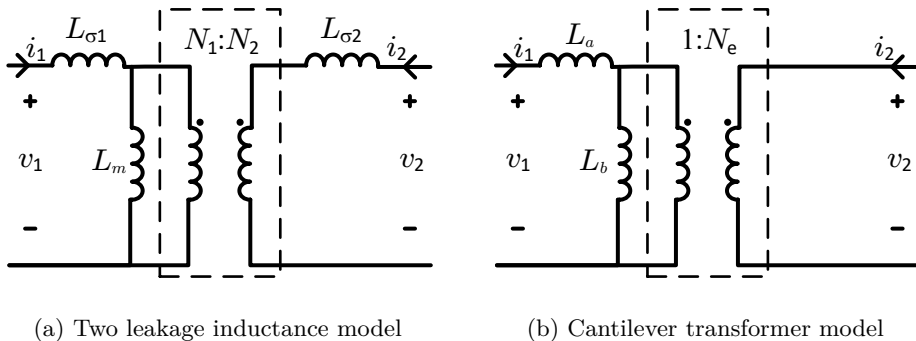
Figure 2.2: Transformer model with one or two leakage inductances

2.1.2 M-Model

From the time domain voltage relation in (2.6), the frequency domain equations for the voltages can be expressed from Laplace transformation as

$$v_1 = j\omega L_1 i_1 + j\omega M i_2$$
$$v_2 = j\omega M i_1 + j\omega L_2 i_2$$

(2.10)

where ω is the angular frequency of the current.

From the frequency domain relations, a circuit representation called the M-Model, which is illustrated in Fig. 2.3, can be formed. The M-model is not
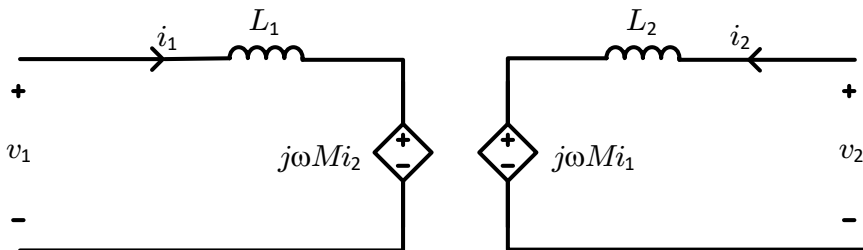
Figure 2.3: M-Model of two coupled inductors with self inductance L_1 and L_2, and mutual inductance M

explicitly dependent on turns number, as the transformer model is. Instead the coupling is described by the mutual inductance and the currents on either side.

2.1.3 T-Model

One of the most frequently used model for compensation analysis is the T-model which can be derived from the M-model. Starting from (2.6) and adding and subtracting $M\frac{\partial i_1(t)}{\partial t}$ and $M\frac{\partial i_2(t)}{\partial t}$ from v_1 and v_2 respectively, it becomes

$$
\begin{aligned}
v_1(t) &= (L_1 - M)\frac{\partial i_1(t)}{\partial t} + M\frac{\partial}{\partial t}\overbrace{(i_1 + i_2)}^{i_m} \\
v_2(t) &= M\frac{\partial}{\partial t}\underbrace{(i_1 + i_2)}_{i_m} + (L_2 - M)\frac{\partial i_2(t)}{\partial t}.
\end{aligned}
\tag{2.11}
$$

The inductances $L_1 - M$ and $L_2 - M$ has no physical interpretation and can even become negative for unsymmetrical coils. The equivalent circuit of the T-model is shown in Fig. 2.4.
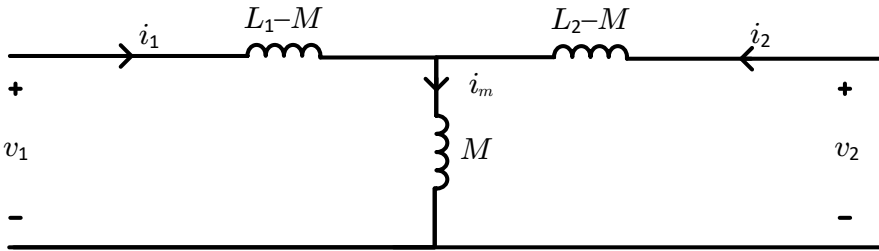
Figure 2.4: T-Model of two coupled inductors with self inductance L_1 and L_2, and mutual inductance M

2.2 Maximum Power Transfer For Uncompensated Coils

For two coupled coils the maximum VA rating can be expressed as the product of open-circuit voltage (V_{oc}) and the short-circuit current (I_{sc}) on the secondary side:

$$
S_u = V_{\text{oc}}I_{\text{sc}}^*
\tag{2.12}
$$

where I_{sc}^* is the complex conjugate of I_{sc}. V_{oc} and I_{sc} can be expressed from (2.10) by setting $i_2 = 0$ and $v_2 = 0$ respectively. The expressions for V_{oc} and I_{sc} then

become

$$V_{\text{oc}} = j\omega M i_1 \tag{2.13}$$

$$I_{\text{sc}} = \frac{M i_1}{L_2}. \tag{2.14}$$

Inserting (2.13) and (2.14) into (2.12) gives

$$S_u = \frac{j\omega M^2 i_1^2}{L_2} = j\omega k^2 L_1 i_1^2 \tag{2.15}$$

and according to the maximum power transfer theorem the maximum output power is $P_o = S_u/2$. This is illustrated in Fig. 2.5 where the normalized output power is plotted for different normalized load resistances $(R_{load}/(\omega L_2))$.
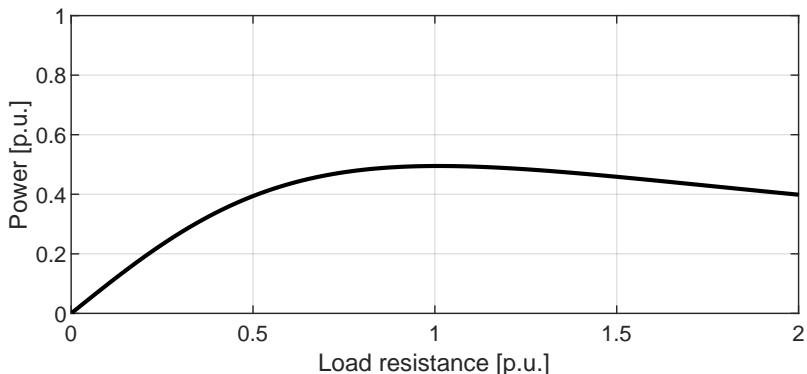
Figure 2.5: Output power for two loosely coupled coils with a resistive load

2.3 Sizing of Coils

In practical applications, one or both of the coils often have limitations regarding size. Recalling the definition of k, defined in (2.7), in order to maximize k the expressions for the mutual and the self inductance needs to be determined. In [32] the expression for mutual inductance is derived for circular coils in free space as

$$M(\rho_1, \rho_2, z) = \mu_0 \sqrt{\rho_1 \rho_2} \left[\left(\frac{2}{k_M} - k_M \right) F(k_M^2) - \frac{2}{k_M} E(k_M^2) \right] \tag{2.16}$$

where $F(k_M^2)$ and $E(k_M^2)$ are the complete elliptical integrals of first and second kind respectively and k_M is the elliptical modulus

$$k_M^2 = \frac{4\rho_1\rho_2}{(\rho_1 + \rho_2)^2 + z^2} \tag{2.17}$$

where ρ_i is the radius of coil with index i and z is the separation between the coils. By setting the secondary radius as $\rho_2 = \rho_1 - r_w$, where r_w is the wire radius, and $z = 0$, the self inductance can be obtained by inserting the parameters in (2.16) and get

$$L_1(\rho_1, r_w) = \mu_0\sqrt{\rho_1(\rho_1 - r_w)}\left[\left(\frac{2}{k_L} - k_L\right)F(k^2) - \frac{2}{k_L}E(k_L^2)\right] \tag{2.18}$$

where the elliptical modulus is

$$k_L^2 = \frac{4\rho_1(\rho_1 - r_w)}{(2\rho_1 - r_w)^2}. \tag{2.19}$$

The coupling factor can then be calculated from (2.7) as

$$k = \frac{M(\rho_1, \rho_2, z)}{\sqrt{L(\rho_1, r_w)L(\rho_2, r_w)}}. \tag{2.20}$$

A comparison of simulated coupling factors for air-core coils and the analytical expression in (2.20) is illustrated in Fig. 2.6. Another way of determining the size of the coils is by calculating the magnetic flux density in the radial, B_ρ, and normal, B_z, direction. The outer radius of the secondary is then determined from when the magnetic flux density in the normal direction, B_z, is zero. The expression for the magnetic flux density from a circular coil to a point P $= (\rho_P, 0, z_P)$ in free space is given by

$$B_\rho(\rho_P, z_P) = \frac{\mu_0 I z_P}{2\pi\rho_P\sqrt{(a - \rho_P)^2 + z_P^2}}\left(\frac{a^2 + \rho_P^2 + z_P^2}{(a + \rho_P)^2 + z_P^2}E(k_B^2) - F(k_B^2)\right) \tag{2.21}$$

$$B_z(\rho_P, z_P) = \frac{\mu_0 I z_P}{2\pi\rho_P\sqrt{(a - \rho_P)^2 + z_P^2}}\left(\frac{a^2 - \rho_P^2 - z_P^2}{(a + \rho_P)^2 + z_P^2}E(k_B^2) + F(k_B^2)\right) \tag{2.22}$$

where ρ_P is the radial distance to the point P and z_P is the separation distance between the coils, a is the radius of the current loop with current I flowing and $E(k_B^2)$ and $F(k_B^2)$ are the complete elliptical integrals of first and second kind respectively. The elliptical modulus k_B^2 is

$$k_B^2 = \frac{4a\rho_P}{2a\rho_P - (a^2 + \rho_P^2 + z_P^2)}. \tag{2.23}$$
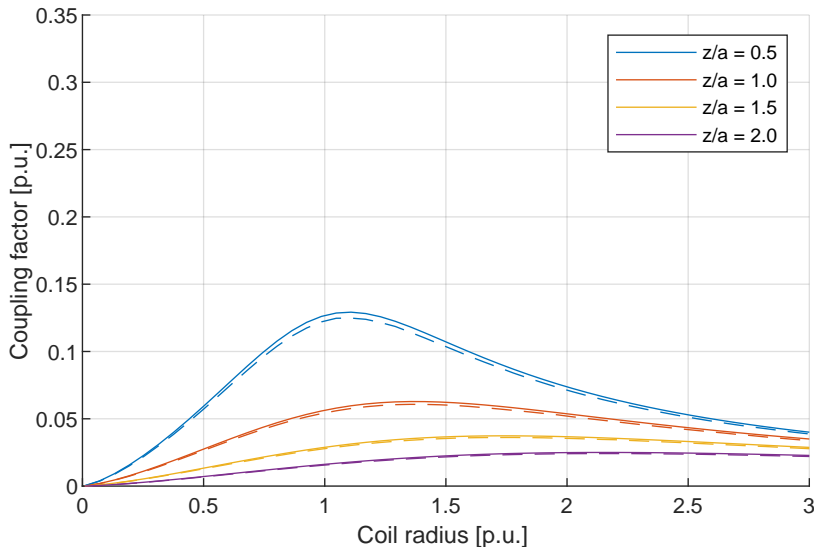
Figure 2.6: Comparison of analytical (solid) and simulated (dashed) coupling factor for two current loops with different air gap-to-radius ratios (z/a) in free space.

The full derivation of this expression is shown in Appendix A. Given the size of a current loop, the expression can be used to determine the size of a second current loop at a distance z_P that maximizes the induced voltage in that loop. The radius, ρ_P, of that current loop will be where $B_z(\rho_P, z_P)$ is zero. The principle is illustrated in Fig. 2.7. Equation (2.22) can also be used to determine the coupling between two current loops, similarly as (2.20).

2.3.1 Influence of Coils in Magnetic Substrates

Magnetic materials, such as ferrites, can be introduced as a substrate behind the coils to increase the inductance and coupling factor. In [33] an approximated expression for the self-inductance with coils in magnetic substrates, accounting for the relative permeability, μ_r, of the magnetic material, is derived

$$L = \frac{2\mu_r}{\mu_r + 1} L_0 \tag{2.24}$$

where L is the self-inductance with the magnetic substrate having relative permeability μ_r, and L_0 is the self-inductance of the air-core coil. The expression
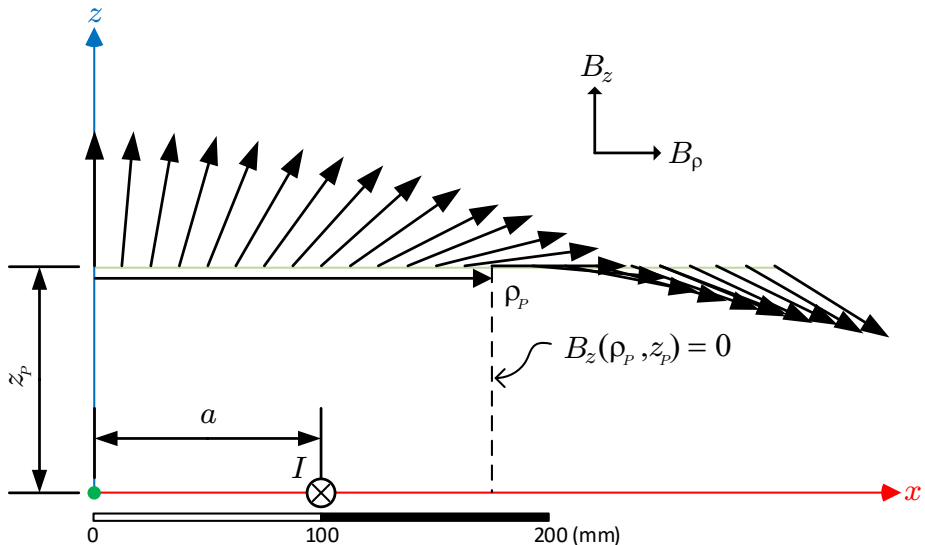
Figure 2.7: Maximizing induced voltage in secondary current loop at ρ_P by solving (2.22) for zero.

is accurate if the distance between the coil and the ferrite is much smaller than the radius of the coil. For any material with relatively high permeability the inductance is in practice doubled since the reluctance path is halved, e.g. with $\mu_r = 100$ the inductance is increased by 98 %. Except for the increase in inductance, the ferrite also contributes to increasing the coupling factor. Comparing Fig. 2.6 without ferrite with Fig. 2.8 where ferrites are placed behind both coils, it can be observed that the coupling factor more than doubles with ferrite. Another important observation is that the radius of maximum coupling is the same whether a magnetic substrate is used or not.

2.4 High Frequency Loss Distribution

The loss contribution due to high frequency can be separated into four parts; skin- and proximity effect in the wires, eddy currents in shielding materials and core losses in the ferrite. The skin effect is caused due to that the current in the circumference of the wire causes a magnetic field that is opposing current to flow in the center of the wire. Similarly as for the internal effect, as for the skin effect, an external field will be generated from the high frequency current in the wire
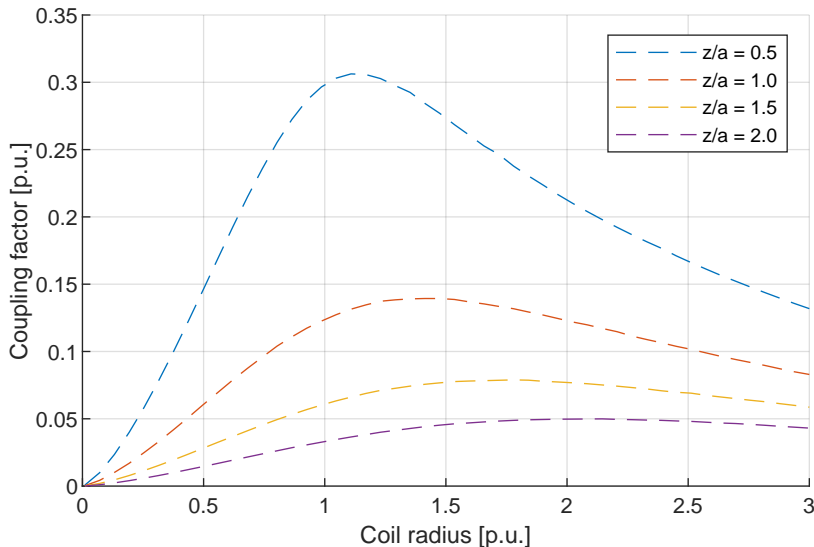
Figure 2.8: Simulated coupling factor for two current loops with a high permeability substrate at different air gap-to-radius ratios (z/a).

that influences the current distribution of wires located in the proximity. The skin- and proximity effect are illustrated in Fig. 2.9.

The current density has an exponential decay from the surface of the conductor. At the distance from the circumference where the current density has decreased by 63 % of the surface current density is called the skin depth, δ. The skin depth can be calculated as

$$\delta = \sqrt{\frac{2\rho_{cu}}{\omega\mu}} \tag{2.25}$$

where ρ_{cu} is the resistivity, $\mu = \mu_0\mu_r$ is the permeability and $\omega = 2\pi f$ where f is the frequency of the current. The additional losses due to skin- and proximity effect are analyzed in [34] and the ratio of ac and dc resistance can be approximated with

$$\frac{r_{ac}}{r_{dc}} = 1 + \frac{\pi^2\omega^2\mu_0^2N^2n_s^2d_s^6K}{768\rho_{cu}^2b^2} \tag{2.26}$$

where N is the number of turns, n_s is the number of strands of the litz wire, d_s is the diameter of one strand, K is to account for multi winding transformer and b is the width of the winding.

Currents are also induced in conductive objects in the vicinity of the coils,

(a) Skin effect at 1 Hz

(b) Skin effect at 100 kHz

(c) Skin- and proximity effect at 100 kHz

Figure 2.9: Illustration of the influence on current distribution due to skin- and proximity effect.

such as the vehicle chassis and coil shielding. These losses are categorized as shielding losses.

2.4.1   Core Losses

The forth loss component from the coupled inductors is the core loss, which are of two parts; hysteresis losses and eddy current losses. Hysteresis losses are due to the hysteresis in the B-H curve of the material. Ferrites have a high resistivity hence the loss contribution from induced eddy currents becomes small. With sinusoidal currents, the core loss density can be estimated with Steinmetz's equation

$$P_v = C_m f^\alpha B^\beta \tag{2.27}$$

where f is the frequency, B is the flux density and C_m, α and β are material constants. The loss density also depends on the temperature, illustrated for some different soft ferrites in Fig 2.10 [35].
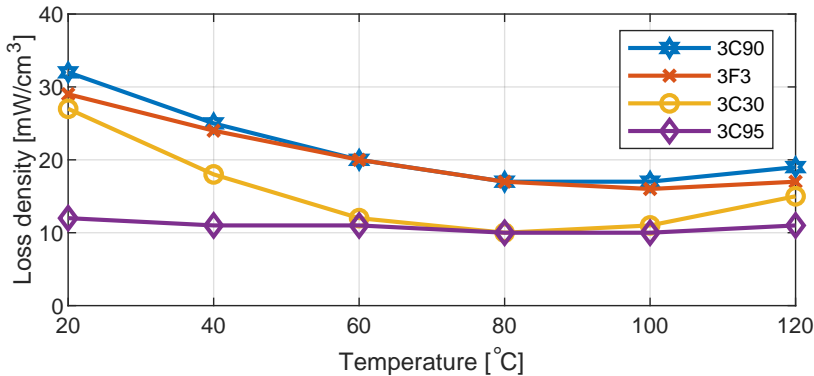
Figure 2.10: Loss density for different ferrites as a function of temperature (B = 50 mT and f = 100 kHz). The data is obtained from [35].

It can be observed that for most materials the minimum loss density occurs at around 80° C. The losses can differ by a factor of two compared to operating at 20° C and hence, it is beneficial to design the cooling of the ferrite to allow for some heating of the ferrite above normal room or outdoor temperatures.

2.5 Summary

The modeling of two coupled coils is presented by three different equivalent models. Firstly, the traditional transformer model with either one or two leakage inductances, commonly used for traditional transformers, is presented. Secondly, the M-model is evaluated. The M-model describes the relation of induced voltage with a mutual inductance between the coils. Lastly, the T-model is derived based on the coupled coils equations in (2.6). All models are electrically equivalent but are described with different parameters. Additionally, the T-model is lacking the galvanic isolation representation, which is explicitly shown in the other models.

Two analytical methods for the derivation of the coil parameters are presented. However, these are restricted to coils in free space. A simple formula showing that for sufficiently high permeability the reluctance path is basically halved leading to a doubling of the inductance. It is also shown that when a high permeability substrate is added to the coils the coupling between them is to a significant extent increased.

Finally, the high frequency losses in the litz wire and in the magnetic materials are analyzed. An expressions for ac losses in the litz wire is presented and Steinmetz's equation are used for estimating the core losses.

CHAPTER 2.

3. Compensation Topologies

As concluded in the previous chapter, the power transfer is very poor if the coupling between the coils is low. Furthermore, the source needs to provide the reactive power for the leakage flux which leads to additional losses in the power electronics. To overcome this, capacitors can be added on either or both sides for reactive power compensation. There are four main compensation topologies where capacitors are added in either series (S) or parallel (P) on both sides. This gives four possible compensation topologies; series-series (SS), series-parallel (SP), parallel-series (PS) and parallel-parallel (PP). The compensation topologies are illustrated in Fig. 3.1 where L_i is the self-inductance of the coils, C_i is the capacitance of the compensation capacitors and r_i is the equivalent series resistance, ESR, of the coils. The subscript i indicates primary ($i = 1$) or secondary ($i = 2$) respectively.

The merits and demerits of each compensation topology have been analyzed in numerous studies, [28–31, 36]. All of the four basic topologies can be modified with an additional inductor or capacitor forming an LCC- or LLC-network resulting in less emissions and better transfer characteristic [30, 37, 38]. The downside is that the due to the additional components the efficiency is decreased [30, 37]. Here the analysis is made for series compensated primary side, yet the same approach is applicable for the other compensation topologies.

3.1 First Harmonic Approximation

The voltage waveform to the primary coil from the inverter is illustrated in Fig. 3.2. Both switches in each leg will be on for 50 %, complementary to the other switch in the same leg. By controlling the phase-shift between the two legs, t_d in Fig. 3.2

(a) Series-series compensation

(b) Series-parallel compensation

(c) Parallel-series compensation

(d) Parallel-parallel compensation
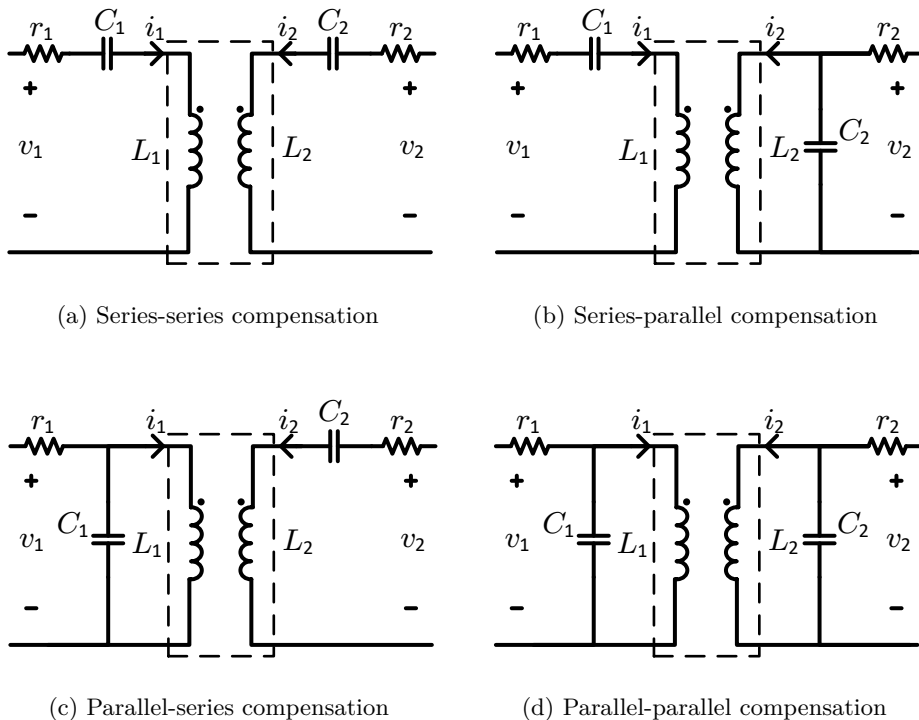
Figure 3.1: The four basic compensation topologies with a single capacitor on either side.

can be changed. A duty cycle, d, can then be introduced as

$$d = \frac{t_d}{T_p/2} \tag{3.1}$$

where t_d is the on-time and T_p is the period time, defined in Fig. 3.2. During the time when both of the upper switches or both of the lower switches are on at the same time the output from the inverter is zero. Correspondingly, when the upper switch in one leg and lower switch in the other leg are on, the dc-link voltage ($\pm V_{dc}$) is applied over the coil.

Since the compensation networks form a resonance circuit tuned for the fundamental component, the only harmonic seen is the switching frequency. To simplify the analysis, the inverter can be replaced with a sinusoidal source with only the fundamental frequency component. This approximation is called first harmonic approximation (FHA) and is further described in [39]. The voltage amplitude of harmonic, n, with duty cycle, d, can be expressed from Fourier
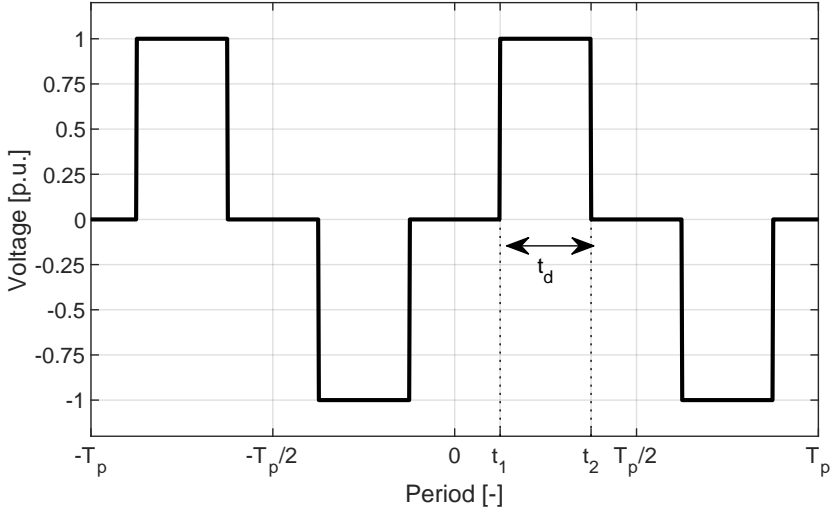
Figure 3.2: Full-bridge inverter output voltage with phase-shift between the legs.

analysis as

$$V_n = \frac{4}{\pi} \frac{V_{dc}}{n} \cdot \left| \sin \left(\frac{n\pi d}{2} \right) \right| \tag{3.2}$$

where V_{dc} is the dc-link voltage, $n = 1, 3, 5, ...$ is the harmonic component and $d = 0 - 100\%$ is the duty cycle, where 0 % corresponds to no phase-shift and 100 % corresponds to a phase-shift of 180°. The time $t_d = t_2 - t_1$ is related to the duty cycle, d, and the period time, T_p, as

$$d = \frac{2t_d}{T_p}. \tag{3.3}$$

The normalized harmonic amplitude, V_n/V_{dc}, for $n = \{1, 3, 5, 7\}$ as a function of duty cycle is plotted in Fig. 3.3.

3.2 Resistive Load Model

If a load resistance, R_L, is connected through a full bridge diode rectifier between the terminals at v_2, in Fig. 3.1, the resistance seen from the input of the diode

Figure 3.3: Harmonic content as a function of duty cycle for the first four harmonics.

rectifier will depend on if it is fed by a voltage or current source as [40]

$$R_{load,i} = \frac{8}{\pi^2} R_L \tag{3.4}$$

$$R_{load,v} = \frac{\pi^2}{8} R_L \tag{3.5}$$

where $R_{load,v}$ is the equivalent resistance seen from a voltage source and $R_{load,i}$ is the equivalent resistance seen 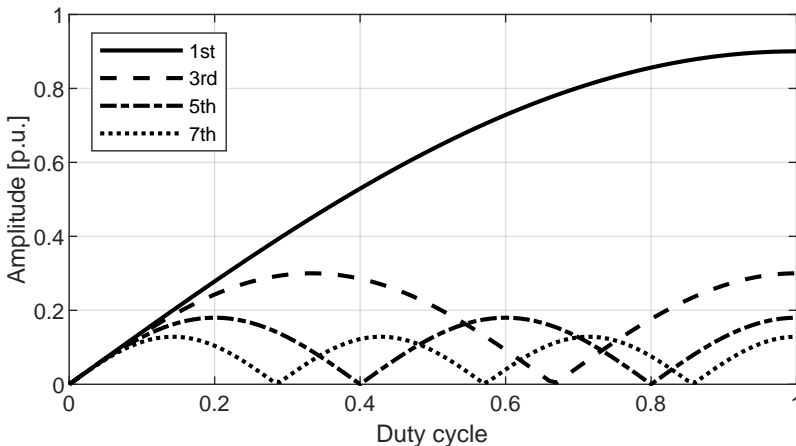from a current source. It will be evident after the upcoming sections that the series-series compensation gives a current source output behavior and (3.4) is applicable. For series-parallel compensation the output will be a voltage source and (3.5) is valid. However, in battery charging applications, the battery is usually modeled with RC-branches in series with a voltage source to describe the time constants of the battery [41]. To simplify the analysis of the IPT system a simplified battery model is used, where the battery is modeled as a resistor which consumes equal amount of power as the battery. The equivalent resistance of the battery load becomes

$$R_L = \frac{V_{bat}^2}{P_{bat}} \tag{3.6}$$

where V_{bat} is the nominal voltage of the battery, and P_{bat} is the charging power determined from the charging current as $P_{bat} = V_{bat} \cdot I_{bat}$. From this the equivalent load resistance can be determined by combining (3.6) with (3.5) or (3.4), depending on the output characteristic. Since the battery voltage, V_{bat}, changes depending on state-of-charge (SoC) of the battery, the resistance, R_L, changes accordingly.

3.3 Series-Series Compensation

The series-series compensation can be tuned to work in constant current operation with zero phase shift, making it suitable for battery charging applications. It can also be tuned to operate with constant voltage output but with lagging power factor. One of the main problems with the series-series compensation is that if there is no load present, the primary side acts as a short circuit for the voltage source which requires additional protection and shutdown system.

The impedance on the primary and secondary side can be expressed as

$$Z_1 = r_1 + j(\omega L_1 - \frac{1}{\omega C_1})$$
$$Z_2 = r_2 + R_{load} + j(\omega L_2 - \frac{1}{\omega C_2}) \tag{3.7}$$

where R_{load} is the equivalent load resistance. In order for the series-series compensated circuit to be operated in load independent constant current, the circuit in Fig. 3.1a can be re-drawn as the M-model, shown in Fig. 3.4. The primary side

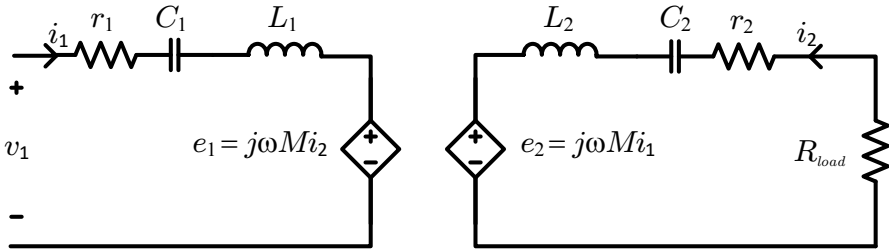Figure 3.4: M-Model of series-series compensated coupled coils

current can then be expressed as

$$i_1 = \frac{v_1 - e_1}{Z_1} \tag{3.8}$$

and the secondary side current is the induced voltage on the secondary side divided by Z_2, so the ratio of the primary to secondary current can be calculated from

$$i_2 = \frac{-j\omega M \cdot i_1}{Z_2}$$
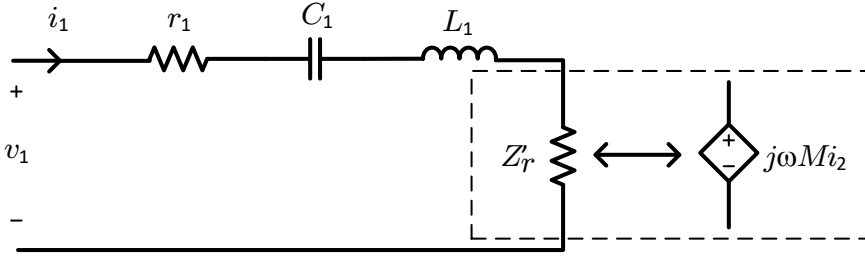$$\frac{i_1}{i_2} = j\frac{Z_2}{\omega M}. \tag{3.9}$$

Figure 3.5: Secondary side impedance reflected to primary side

The expression for i_2 then becomes

$$i_2 = -\frac{e_2}{Z_2} = -\frac{j\omega M}{Z_2}i_1 = -\frac{j\omega M}{Z_2}\frac{v_1 - e_1}{Z_1} = -\frac{j\omega M}{Z_1 Z_2}(v_1 - j\omega M i_2)$$

$$\Rightarrow i_2 \frac{Z_1 Z_2 + (\omega M)^2}{Z_1 Z_2} = -\frac{j\omega M v_1}{Z_1 Z_2}$$

$$\Rightarrow i_2 = -\frac{j\omega M v_1}{Z_1 Z_2 + (\omega M)^2}$$

and if ω is chosen to

$$\omega = \frac{1}{\sqrt{L_1 C_1}} \tag{3.10}$$

then $\text{Im}\{Z_1\} = 0$. For small values of r_1, such that $r_1 Z_2 \ll (\omega M)^2$, (3.10) can be approximated as

$$i_2 \approx \frac{v_1}{j\omega M}. \tag{3.11}$$

From (3.11) it can be noted that the secondary current is lagging the primary voltage by approximately 90 degrees and the value of Z_2 does not influence the secondary current. Although, to maximize the efficiency, the source voltage and current should be in phase. The secondary impedance Z_2 can be reflected to the primary side, illustrated in Fig. 3.5 and the reflected impedance, Z_r', becomes

$$Z_r' = \frac{e_1}{i_1} = j\omega M \frac{i_2}{i_1} = j\omega M \frac{-j\omega M}{Z_2} = \frac{(\omega M)^2}{Z_2}. \tag{3.12}$$

The transferred impedance, Z_r', should be purely resistive in order for the source voltage and current to be in phase. From (3.12) it can be observed that $\text{Im}\{Z_r'\} = 0 \Rightarrow \text{Im}\{Z_2\} = 0$ which leads to $L_2 C_2 = L_1 C_1$. Hence, the secondary capacitor should be chosen similarly as for the primary side, as in (3.10). The input current can then be expressed as

$$i_1 = \frac{v_1}{r_1 + Z_r'} = \frac{v_1}{r_1 + \frac{(\omega M)^2}{Z_2}} = \frac{v_1 Z_2}{r_1 Z_2 + (\omega M)^2} \tag{3.13}$$

where $Z_2 = r_2 + R_{load}$. From (3.7) and (3.12) the total input impedance with compensated self inductances can be written as

$$Z_{ss} = \text{Re}\{Z_1\} + \text{Re}\{Z'_r\} = r_1 + \frac{(\omega M)^2}{(r_2 + R_{load})}.$$ (3.14)

The second term is, for normal operation points, much larger than the first term.

3.3.1 Power Transfer and Maximum Efficiency for Series-Series Compensated Coils

With tuned coils according to the previous section, the current and voltage will be in phase and $\text{Im}v_1 = \text{Im}i_1 = 0$. The input and output power can then be calculated as

$$\begin{aligned} P_{in,ss} &= v_1 i_1 = \frac{v_1^2 Z_2}{r_1 Z_2 + (\omega M)^2} \\ P_{out,ss} &= P_{Z_r} \cdot \frac{R_{load}}{Z_2} = Z'_r \cdot i_1^2 \cdot \frac{R_{load}}{Z_2} \\ &= \frac{(\omega M)^2}{Z_2} \cdot \frac{v_1^2 Z_2^2}{(r_1 Z_2 + (\omega M)^2)^2} \cdot \frac{R_{load}}{Z_2} \\ &= \frac{v_1^2 (\omega M)^2 R_{load}}{(r_1 Z_2 + (\omega M)^2)^2} \end{aligned}$$ (3.15)

where P_{Z_r} is the power delivered to the reflected impedance Z'_r and $Z_2 = r_2 + R_{load}$. The maximum output power can be expressed from the output open-circuit voltage and short-circuit current, as for the uncompensated coil. The open-circuit voltage and the short circuit current becomes

$$V_{oc} = j\omega M i_1$$ (3.16)

$$I_{sc} = \frac{j\omega M i_1}{r_2}$$ (3.17)

and the maximum output power for series-series compensation, $S_{c,ss}$, becomes

$$S_{c,ss} = V_{oc} I^*_{sc} = \frac{(\omega M i_1)^2}{r_2} = \frac{\omega M^2 i_1^2 Q_2}{L_2}$$ (3.18)

which is a factor of Q_2 higher than the uncompensated power transfer in (2.15). The factor Q_2 comes from that the short circuit current is increased with series-series compensation. Furthermore, for the uncompensated coils, the load was matched to the reactance of the secondary coil, ωL_2, for maximum power transfer, leaving only half of the apparent power (as was illustrated in Fig. 2.5). In this

case the reactive power is compensated, giving an additional factor of 2 for active power transfer.

Since $\text{Im}\{Z_1\} = \text{Im}\{Z_2\} = 0$, the efficiency can be expressed from (3.15) as

$$\eta_{ss} = \frac{P_{out,ss}}{P_{in,ss}} = \frac{R_{load}}{r_2 + R_{load}} \frac{k^2 Q_1 Q_{2,L}}{1 + k^2 Q_1 Q_{2,L}} \tag{3.19}$$

where Q_1 is the native quality factor of the primary coil, and $Q_{2,L}$ is the loaded quality factor of the secondary side. It is persuasive to expect that the higher R_{load}, the higher the efficiency. However, $Q_{2,L}$ is also influenced by changing R_{load}. Instead, to evaluate the optimal load in terms of efficiency (3.19) can be differentiated with respect to R_{load}. Firstly, η_{SS} is written out explicitly declaring the dependence of R_{load},

$$\eta_{SS} = \frac{R_{load}(\omega M)^2}{r_1(R_{load} + r_2)^2 + r_2(\omega M)^2 + R_{load}(\omega M)^2}. \tag{3.20}$$

The differentiation of (3.20) with respect to R_{load} can then be set to zero and solved for the optimal value of the load:

$$\frac{\partial \eta_{ss}}{\partial R_{load}} = (\omega M)^2 \frac{\left(\begin{array}{c} R_{load}^2 r_1 + R_{load}(2r_1 r_2 + (\omega M)^2) + r_2(r_1 r_2 + (\omega M)^2) - \\ R_{load}(2R_{load} r_1 + 2r_1 r_2 + (\omega M)^2) \end{array} \right)}{(R_{load}^2 r_1 + R_{load}(2r_1 r_2 + (\omega M)^2) + r_2(r_1 r_2 + (\omega M)^2))^2}$$

$$= 0$$

$$\Rightarrow R_{load,opt} = \sqrt{\frac{r_1 r_2^2 + r_2(\omega M)^2}{r_1}} = r_2\sqrt{1 + k^2 Q_1 Q_2} \tag{3.21}$$

where Q_1 and Q_2 are the native quality factors of the coils. For $k^2 Q_1 Q_2 >> 1$, the optimal load can be expressed as

$$R_{load,opt} = r_2\sqrt{1 + k^2 Q_1 Q_2} \overset{[k^2 Q_1 Q_2 >> 1]}{\approx} kr_2\sqrt{Q_1 Q_2} = \omega M \sqrt{\frac{r_2}{r_1}} \tag{3.22}$$

which implies that if $k^2 Q_1 Q_2 \gg 1$ the losses should be equally distributed on the primary and secondary side for the optimal loading condition. Inserting $R_{load,opt}$ from (3.21) in (3.20) gives the maximum efficiency

$$\eta_{max,ss} \approx \frac{k^2 Q_1 Q_2}{(1 + \sqrt{1 + k^2 Q_1 Q_2})^2}. \tag{3.23}$$

3.4   Series-Parallel Compensation

For the series-parallel compensation the most common tuning strategy is constant voltage output which is suitable for charging applications where the battery voltage is not changing much over the charging range. If $r_2 \ll R_{load}$ the secondary side can be transformed into the circuit in Fig. 3.6, which is a current fed, parallel RLC-circuit.
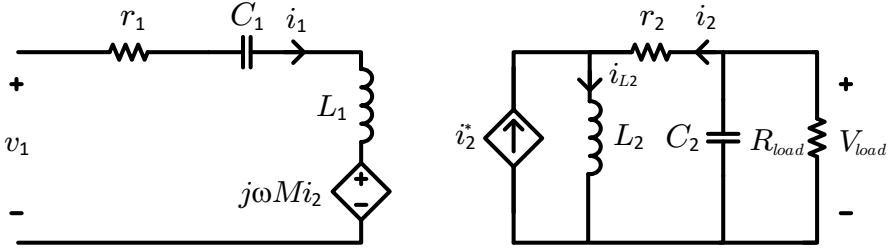
Figure 3.6: The secondary side with source transformed induced voltage into a current source

3.4.1   Zero Phase Angle Tuning

In order to ease the calculation the series resistance of the secondary coil, r_2, is neglected for the tuning. The reflected impedance seen from the primary side then becomes

$$i_2 = i_{L2} - i_2^* = \frac{V_{load}}{j\omega L_2} - \frac{j\omega M i_1}{j\omega L_2} = \frac{M i_1}{L_2}\frac{R_{load}}{j\omega L_2} - \frac{M i_1}{L_2} =$$

$$= i_1\left(\frac{M R_{load}}{j\omega L_2^2} - \frac{M}{L_2}\right) \tag{3.24}$$

$$Z_r' = \frac{e_1}{i_1} = j\omega M\frac{i_2}{i_1} = \frac{k^2 L_1 R_{load}}{L_2} - j\omega L_1 k^2 = k^2\left(\frac{L_1}{L_2}R_{load} - j\omega L_1\right). \tag{3.25}$$

The reflected impedance can be seen as a resistor in series with a negative inductance, proportional to the square of k. Neglecting the series resistance of the coils (r_1 and r_2), the total impedance seen from the input becomes

$$Z_{tot} = \frac{1}{j\omega C_1} + j\omega L_1 - j\omega L_1 k^2 + k^2\frac{L_1}{L_2}R_{load} \tag{3.26}$$

and for zero phase angle (ZPA) tuning the imaginary part of (3.26) should be zero:

$$\text{Im}(Z_{tot}) = -\frac{1}{\omega C_1} + \omega L_1 - \omega L_1 k^2 = 0 \tag{3.27}$$

or equivalently

$$C_1 = \frac{1}{\omega^2 L_1 (1 - k^2)}. \tag{3.28}$$

This results in that the resonance frequency is dependent on the coupling between the coils. The total impedance seen from the primary side with a coupling factor k_0 that gives ZPA, can then be written as

$$Z_{sp} = k_0^2 \frac{L_1}{L_2} R_{load}. \tag{3.29}$$

3.4.2 Power Transfer and Maximum Efficiency for Series-Parallel Compensated Coils

The maximum power transfer for series-parallel compensated coils can be determined in a similar way as for series-series compensated coils. In the case of series-series compensation the short circuit current was increased by Q. For the series-parallel tuning the open-circuit voltage is instead increased by a factor of Q. The expression for the output power then becomes the same as for series-series compensation [42]

$$S_{c,sp} = \frac{\omega M^2 i_1^2 Q_2}{L_2} \tag{3.30}$$

This indicates that the series-series is more suitable for high current operation or more turns while the series-parallel is more suitable for high voltage operation or less turns.

With $Q_1 Q_2 \gg 1$ the expression for the maximum efficiency of the series-parallel compensated circuit becomes the same as for series-series [30, 36],

$$\eta_{max,sp} \approx \frac{k^2 Q_1 Q_2}{(1 + \sqrt{1 + k^2 Q_1 Q_2})^2} \tag{3.31}$$

where Q_1 and Q_2 are the native quality factors of the coils.

3.5 Bifurcation

At some conditions the system can have several ZPA frequencies or resonant frequencies. This phenomena is called bifurcation. It occurs when the reflected

impedance is high in comparison to the primary self inductance [28], i.e. when the coupling factor is high or the load resistance is small. The ZPA frequency is then split into three frequencies, one above, f_H, and one below, f_L, the center resonance frequency f_o. An illustration of the voltage gain for series-series compensated coils with $Q_1 = Q_2 = 400$ and $k = 0.15$ is shown for different loaded quality factors in Fig. 3.7. Bifurcation can be observed in the phase of the input impedance.
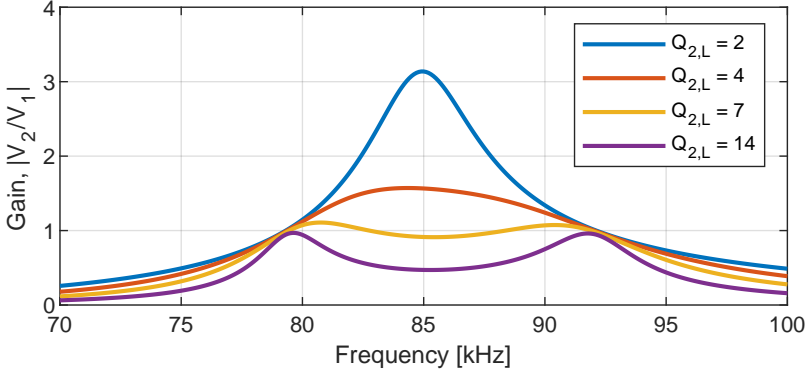
Figure 3.7: Bifurcation phenomena for the voltage gain.

If bifurcation-free operation is achieved, an increase in the switching frequency from the resonance frequency would result in a more inductive load seen from the inverter. However, for bifurcation, an increase in the switching frequency leads to a capacitive load and capacitive switching. With capacitive switching, zero voltage switching (ZVS) can not be fulfilled and the switching losses will increase significantly. The phase of the load seen by the inverter for the same operation points as above is shown in Fig. 3.8.

The critical coupling factor, k_{crit}, is the maximum coupling factor which bifurcation-free operation is achieved. For series-series compensation it has been shown in [28, 43, 44] to be

$$k_{crit} = \frac{1}{Q_{2,L}} \sqrt{1 - \frac{1}{4Q_{2,L}^2}}. \tag{3.32}$$

In Fig. 3.9 the relation in (3.32) is illustrated for k_{crit} and $Q_{2,L}$. In the previous example the coupling factor is $k = 0.15$. This corresponds to a maximum loaded quality factor of $Q_{L,2,max} = 7$ for bifurcation-free operation.
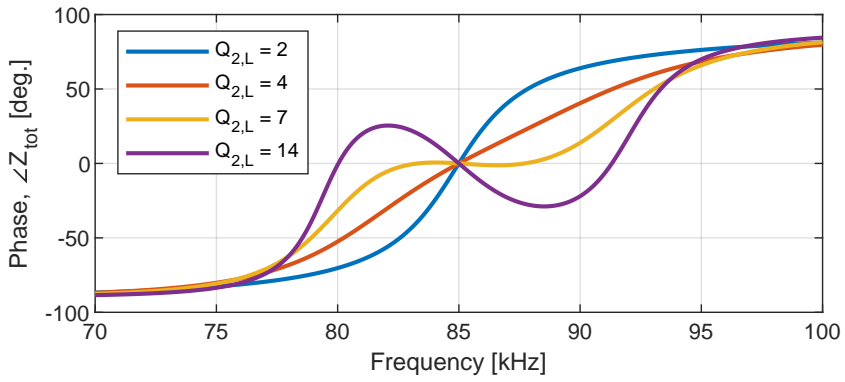
Figure 3.8: Phase of the impedance seen from the inverter for different quality factors and frequencies.
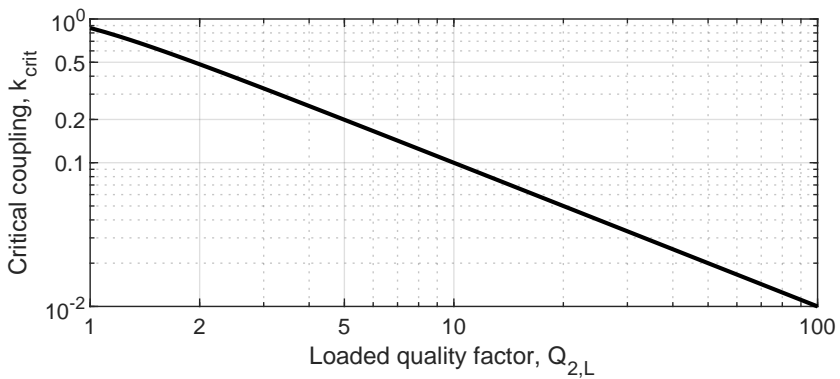
Figure 3.9: Critical coupling for different loading conditions in terms of loaded quality factor.

3.6 Summary

In order to increase the efficiency and maximum power transfer capability for loosely coupled coils, compensation networks can be added on both sides. The use of a first harmonic approximation of the voltage from the inverter and a linearized load model is motivated.

The series-series and series-parallel compensation topologies are analyzed and it is shown that from a maximum power transfer and maximum efficiency perspective, these compensation topologies are equal. The main drawback of the series-series compensation is the short circuit characteristic of the primary side if the load side is left open. For the series-parallel compensation, the main drawback is the coupling dependent compensation.

Lastly, the bifurcation and frequency splitting phenomena is illustrated where the input characteristic and resonance frequency splits into side bands. These phenomena needs to be taken into account from a stability and efficiency point of view when designing IPT systems.

CHAPTER 3.

4. Home Charging System

In this chapter the design and results of a wireless charger for a plug-in hybrid electric vehicle (PHEV) is presented. A ground assembly (GA) containing the primary coil and primary side compensation is placed on the ground. On the PHEV a vehicle assembly (VA) is mounted, containing the secondary coil, secondary side compensation and an output rectifier.

4.1   System Specifications

The single phase IPT charger power level is based on a single phase 230 V outlet with current limited to 16 A. With unity power factor this corresponds to an input power of 3.7 kW and with a system efficiency of 90 % the output power becomes approximately 3.3 kW. The space on the vehicle is limited and in order to ease the mounting and to fit the VA, the outer dimensions are limited to 429 mm × 429 mm. A summary of the system specifications is shown in Tab. 4.1.

Due to the variations in state-of-charge (SoC) of the battery it is beneficial to compensate the coils with series-series compensation. With series-series compensation the resonance frequency will be independent of both the load and the coupling factor (see Chapter 3.3). The inductances (or quality factors) of the coils should be designed in such way that the optimal resistance, $R_{load,opt}$, is in the lower range of the operating region. This is beneficial since the change in efficiency is less for load resistances larger than the optimal resistance compared to lower. Recalling the expression for optimal load in (3.21) and assuming similar primary and secondary inductances ($L_1 \approx L_2$) and coil resistances ($r_1 \approx r_2$), the optimal

Table 4.1: Summary of system parameters and battery specifications

System specifications			
Input power	3.7 kW	Output power	3.3 kW
Efficiency	90 %	VA size	429 mm × 429 mm
Ground clearance	250 mm	Coupling factor min.	0.1
Misalignment	±100 mm	Coupling factor max.	0.15
Battery specifications			
Total pack energy		8.8 kWh	
State-of-Charge (SoC) window		15 % - 90%	
Available pack energy		6.5 kWh	
Battery voltage range		269 V - 398 V	

load can be expressed as

$$
\begin{aligned}
R_{load,opt} = r_2\sqrt{1 + k^2 Q_1 Q_2} &\approx k\sqrt{r_2^2 Q_1 Q_2} \\
&\approx k\sqrt{r_1 r_2 Q_1 Q_2} = k\omega L = \omega M
\end{aligned}
\tag{4.1}
$$

where L is geometric mean of the self-inductances.

The optimal load, $R_{load,opt}$, can be set arbitrary in the operating region based on the voltage of the battery. Here it assumed that the nominal battery voltage is 300 V which from (3.4) and (3.6) gives an equivalent load resistance

$$
R_{load} = \frac{8}{\pi^2}\frac{V_{bat}^2}{P_{bat}} = \frac{8}{\pi^2}\frac{300V^2}{3300W} = 22\Omega.
\tag{4.2}
$$

The inductance value that gives $R_{load,opt} = 22\Omega$ can be determined by rearranging (4.1) as

$$
L = \frac{R_{load,opt}}{k\omega} = \frac{22\Omega}{0.15 \cdot 2\pi \cdot 85kHz} = 275\mu H.
\tag{4.3}
$$

The efficiency for different load resistances are plotted in Fig. 4.1 with optimized efficiency at $R_{load} = 22$ Ω or equivalently $V_{bat} = 300$ V. The highlighted area corresponds to the equivalent load resistance in the SoC window of the battery. It can be seen that if the load resistance is below 10 Ω the efficiency drops rapidly. This corresponds to a battery voltage of approximately 200 V which is well below the lowest battery voltage.
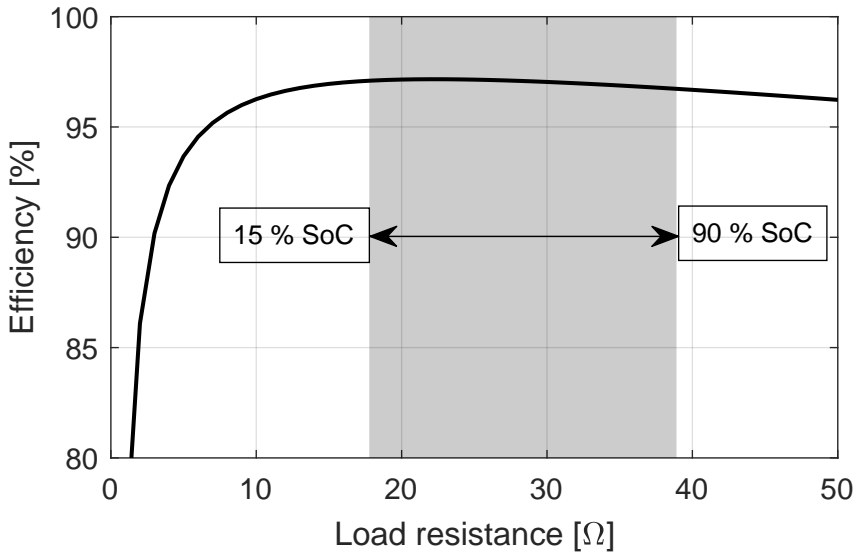
Figure 4.1: Coil-to-coil efficiency for different load resistances. The equivalent load resistance in the SoC window of the battery is highlighted

4.2 Power Electronic Design Considerations

The output of the charger is connected to a variable resistive load through a diode rectifier and the input dc-link is supplied either from the grid through an interleaved power factor correction (I-PFC) rectifier or by two series connected power supplies. The specifications of the power electronics and the electronic load is presented in Tab. 4.2 and a picture of the I-PFC rectifier and inverter is shown in Fig. 4.2.

4.2.1 Zero Voltage Switching

With a high switching frequency it is crucial to minimize the switching losses to achieve a high efficiency. If the self inductance is slightly under compensated, i.e. the full-bridge inverter sees an inductive load, the inductive current can charge the output capacitance, C_{oss}, of the MOSFET at the switching transition. With enough energy stored in the inductive load the MOSFET can be switched-on with zero voltage (ZVS). In order to achieve ZVS, the following relation needs to be

Table 4.2: Specifications of I-PFC and power supply

|	I-PFC rectifier	Power supply
Manufacturer	N/A	Delta SM300-20
Input voltage	120-230 V	342-457 V
Output voltage	390 V	0-300 V
Maximum power	4 kW	6 kW
Power factor	0.99	0.98
Efficiency	96 %	89 %
Inverter		
MOSFET	Voltage	650 V
SCT3022AL	Current	93 A
	$R_{ds,on}$ @ 25 °C	22 mΩ
	C_{oss}	118 pF
	Maximum junction temperature	175 °C
Gate driver	Gate voltage	+19/-4 V
IXDN609PI	Peak output current	±9 A
	Turn on rise time	40 ns
	Turn off fall time	30 ns
Electronic load		
Manufacturer	Elektro-Automatik EL 9750-50	
Input voltage range	0 - 750 V	
Input current range	0 - 50 A	
Resistance	0 - 40 Ω, 0 - 400 Ω	
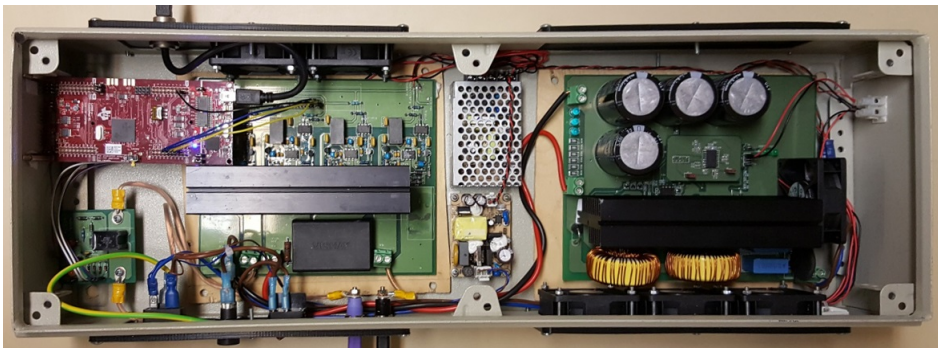
Figure 4.2: PFC rectifier and full-bridge inverter

fulfilled [45]

$$\frac{1}{2}LI_{rms}^2 > \frac{1}{2}\frac{8}{3}C_{oss}V_{dc}^2 \tag{4.4}$$

where L is the inductance seen from the inverter, I_{rms} is the current in the primary side, C_{oss} is the output capacitance of one MOSFET and V_{dc} is the dc-link voltage. In this case the parasitic capacitance of the transformer is neglected.

4.3 Simulation Results

4.3.1 Coil Design

The outer dimensions of the VA is determined by the available space on the vehicle. To achieve the desired inductance an iterative FEM simulation is carried out. Firstly, a ferrite plate with the size 429 mm × 429 mm is assumed. A single rectangular turn is placed such that the area enclosed by the turn is equal to the ferrite area that is not enclosed by the turn. Turns are then added and the position of the turns are adjusted to have equal area of ferrite enclosed and not enclosed. When the desired inductance value is obtained the equivalent radius of the primary coil, ρ_1, can calculated by maximizing (2.20). The same procedure is then repeated for the primary coil.

The final design of the coils is shown in Fig. 4.3 where aluminum rims and an aluminum backplate are added for shielding. Due to symmetry and computational limitations only one forth of the model is simulated hence this FE model is restricted to aligned coils. Each turn of the coil is modeled individually to get a more accurate result of the self-inductance, since the coupling is not perfect between the turns. The mesh of the FEM model contains 1.4 million elements. A summary of the GA and VA design is presented in Tab. 4.3.

The maximum coil-to-coil efficiency can be calculated from (3.23). With quality factors, $Q_1 \approx Q_2 \approx 587$ and a coupling factor, $k = 0.15$, the maximum efficiency is $\eta_{ss} = 97.8\%$. This only accounts for the losses in the coils and if the efficiency of the inverter and rectifier are assumed to be 98 % the system efficiency becomes $\eta_{tot} = 95.8\%$.
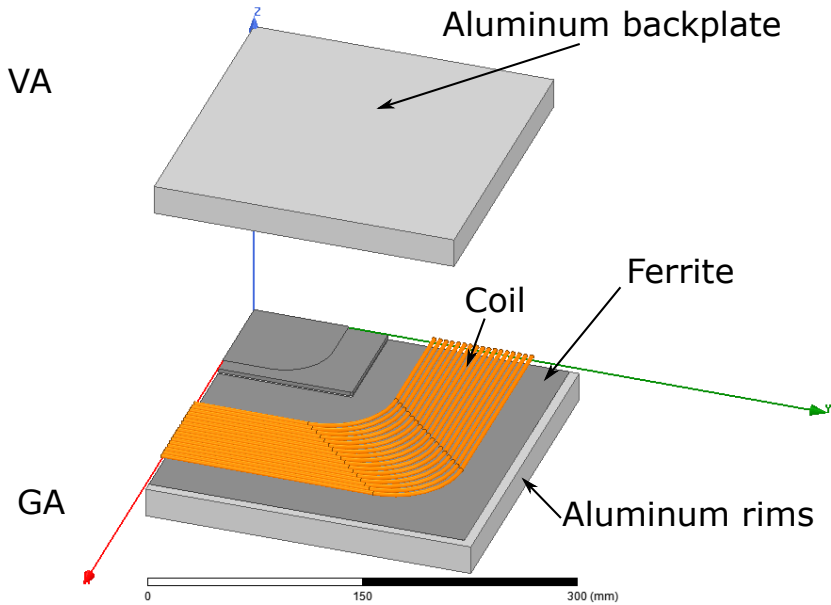
Figure 4.3: 3D FE model of the 3.7 kW GA and VA

4.3.2   System Circuit Simulations

With the parameters presented in Tab. 4.3 a circuit simulation of the system including the inverter and output full-bridge rectifier is done. The power transfer is controlled either by changing the dc-link voltage on the primary side or by changing the duty cycle of the inverter. The voltage- and current waveforms with a dc-link voltage of 390 V and 65 % duty cycle are shown in Fig. 4.4. It can be observed that the primary current and voltage are in phase and that only the fundamental component of the voltage is seen in the current waveform. The switching transient in one MOSFET is shown in Fig. 4.5 where the drain-source voltage, V_{ds}, is charged to zero before the gate signal is turning on the MOSFET. The simulated dc-dc efficiency for the system at the rated operating point is 94.7 %.

4.3.3   Stray Field Simulations

There are no simple methods to calculate the field distribution analytically when the coils are located in a surrounding of electrically or magnetically conducting
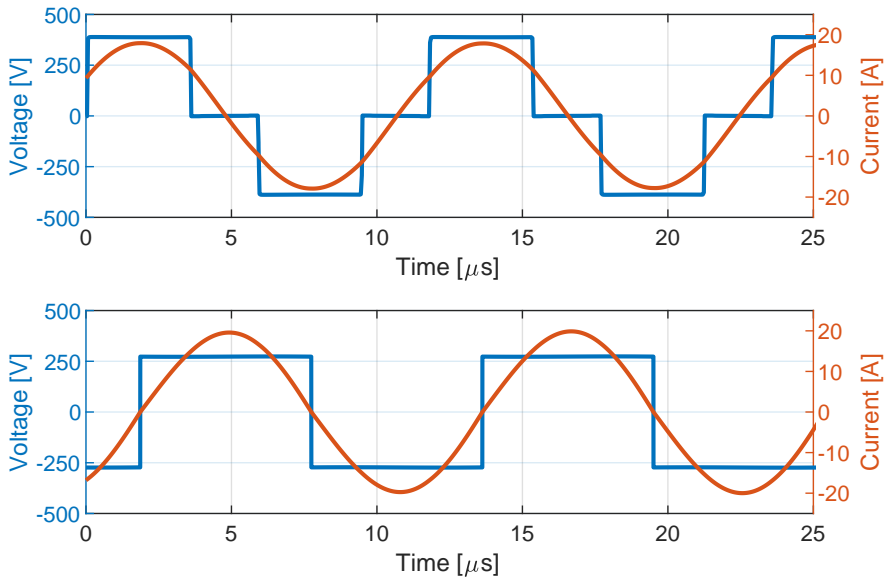
Figure 4.4: Simulated waveforms of IPT charger with 65 % duty cycle and 22 Ω resistive load. Primary voltage and current (top), secondary voltage and current (bottom).
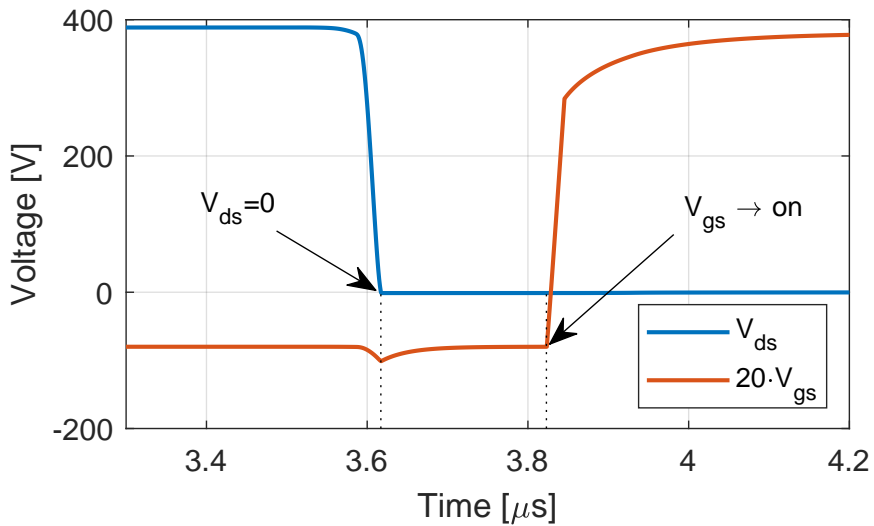

Figure 4.5: Voltage over upper MOSFET during switching. ZVS is fulfilled since the drain-source voltage (V_{ds}) is zero when the transistor is turned on.

Table 4.3: Parameters of GA and VA

	GA	VA
Size (w × l × h)	$466 \times 466 \times 34$ mm	$429 \times 429 \times 34$ mm
Weight	9 kg	5 kg
Wire length	21.6 m	21.2 m
Number of turns	17	20
Inductance	$L_1 = 274\ \mu H$	$L_2 = 271 \mu H$
Coil resistance	$r_{ac,1} = 250$ mΩ	$r_{ac,2} = 246$ mΩ
Capacitance	$C_1 = 12.9$ nF	$C_2 = 12.9$ nF
Quality factor	$Q_1 = 587$	$Q_2 = 586$
Components		
Capacitors	Capacitance	4.7 nF $\pm 10\%$
B32652A2472K	Voltage rating (T < 85 °C)	700 V
	Unit layout, (series × parallel)	4×11
	Total capacitance	$C_1 = C_2 = 12.9$ nF
Litz wire	Strand diameter	$d_s = 0.100$ mm
Polysol 155	Number of strands	$n_s = 240$
	Maximum temperature	155 °C
Ferrite	Relative permeability	$\mu_r = 2000$
PLT38/25/3.8, 3F3	Loss density (100 mT, 100 kHz)	121 mW/cm^3
Cover	Maximum temperature	120 °C
Polycarbonate		

materials such as metals, steel or ferrites. The magnetic flux density in (2.21) and (2.22), presented in Chapter 2, are only valid in free space. FEM software can instead be used to numerically simulate the field distribution around the coils. However, a vehicle has a very complex structure and the volume is large. A more practical solution is to represent the vehicle by a steel sheet above the VA.

The magnetic field is simulated in FEM with two simulation models. One model has only the two coils and the other has a steel sheet, representing the chassis of the vehicle, above the VA. Both models are simulated with rated current, $i_1 = 13.2A$. The flux densities are shown in Fig. 4.6a and Fig. 4.6b for the non-shielded and shielded model respectively. It can be observed that the field distribution is significantly reduced above the two coils with shielding.

For the model with shielding, the magnetic flux density is also simulated
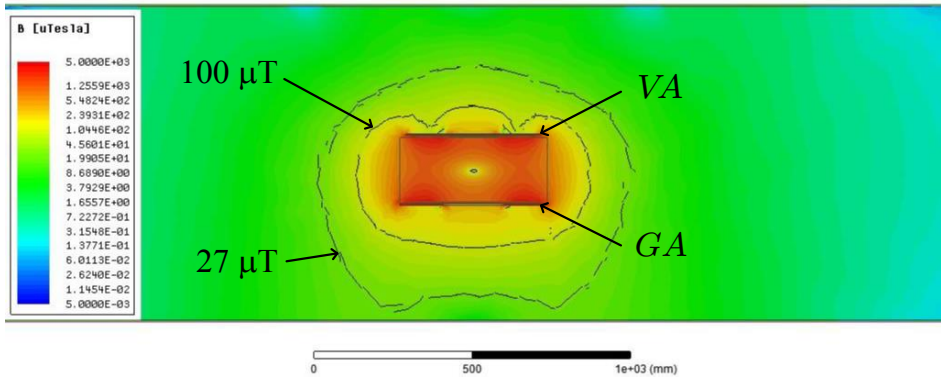
(a) Magnetic flux density distribution without shielding
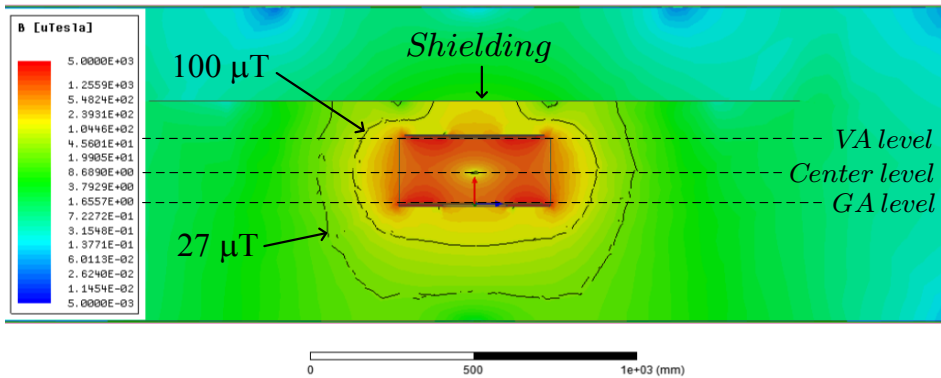
(b) Magnetic flux density distribution with shielding

Figure 4.6: 3D FEM simulation of magnetic flux density without shielding (a) and with a steel sheet representing the PHEV (b)

along the three lines indicated in Fig. 4.6b as 'VA level', 'Center level' and 'GA level'. The flux densities along the three levels are plotted in Fig. 4.7.

The width of the vehicle is 2 m and this area is not considered to be publicly accessible. It can be observed that the flux density is below the public exposure limit approximately 500 mm from the center of the coils which is located at the center of the vehicle. At either side of the vehicle the flux density has decreased to approximately 1 μT. Furthermore, the two peaks on the 'GA level' and 'VA level' curves corresponds to the inner and outer turn of the GA and VA coil respectively. At these points the flux density reaches approximately 10 mT.
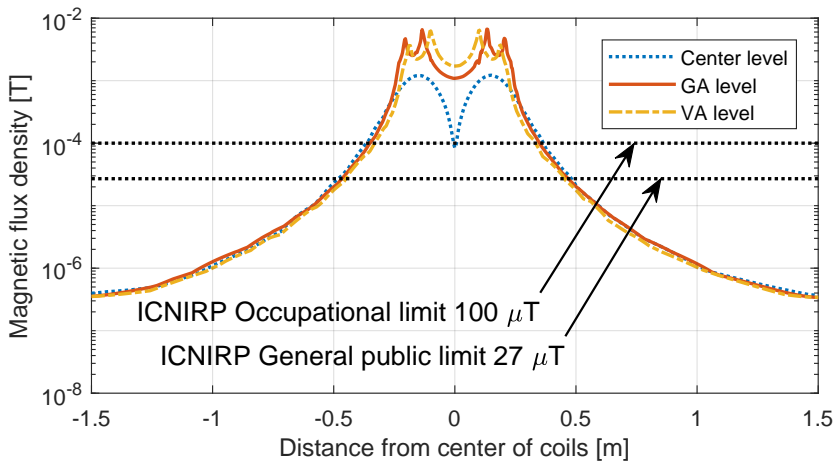
Figure 4.7: Magnetic flux density along the GA level (z= 0 mm), center level (z = 105 mm) and VA level (210 mm)

4.4   Experimental Verification

Two coil-forms of polycarbonate are milled with traces for the coils. Aluminum rims with a 2 mm thick aluminum sheet as backplate are mounted to the coil-forms. Inside the assemblies, I-core ferrites and the compensation capacitors are mounted. Additionally, in the VA a full-bridge rectifier is also mounted, with the aluminum backplate as a heat sink. An exploded view of the VA is shown in Fig. 4.8.

Two L-shaped aluminum profiles are mounted on two sides of the rims in order to fix the VA on the vehicle. With the VA mounted the ground clearance, and hence the air gap, is 210 mm. A photograph of the VA mounted on the vehicle is shown in Fig. 4.9.

Measurements of the self-inductances is done without the compensation capacitors connected and supplying each coil with a square wave voltage. The dc voltage and current are measured and from the slope of the current the self-inductance is obtained. An illustration of the measurement is shown in Fig. 4.10. The self-inductances of the coils are measured to $L_1 = 278$ μH and $L_2 = 276$ μH.
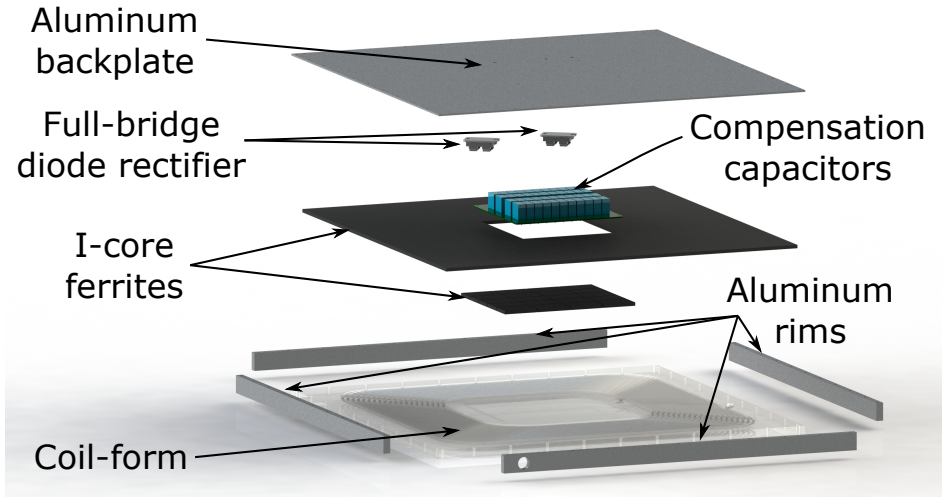
Figure 4.8: Exploded view of the VA
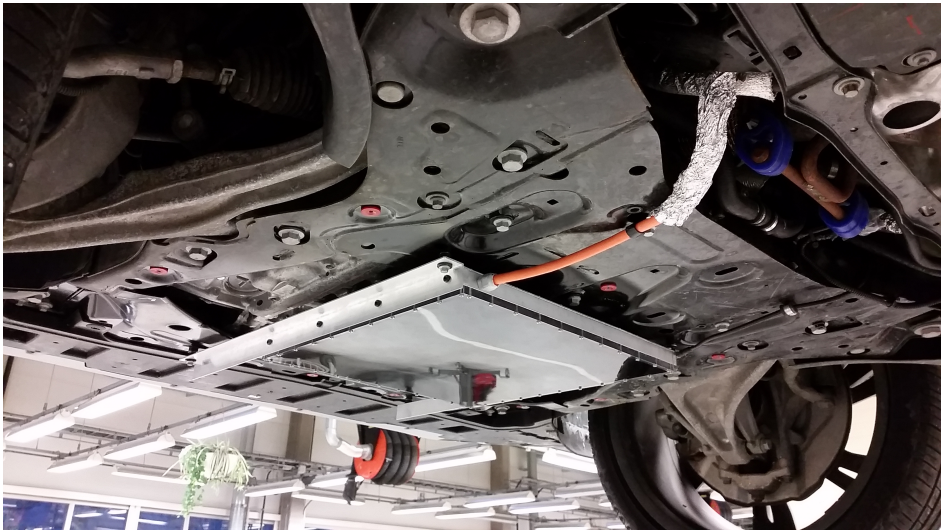
Figure 4.9: Picture of the mounted VA
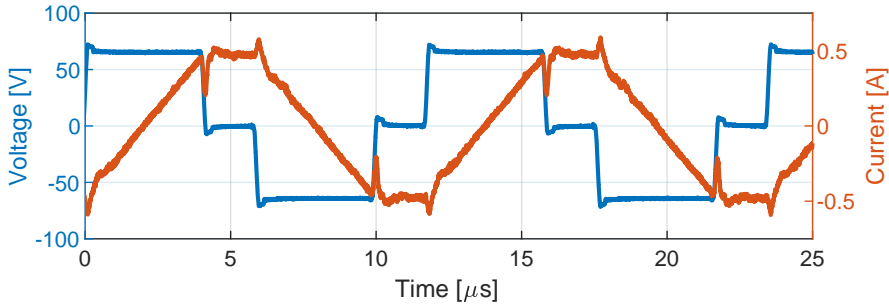
Figure 4.10: Inductance measurement of coil

4.4.1 Control Strategies

The control approach for the system is to keep the primary side coil current fixed at 13.2 A. Here this is achieved with open loop control, changing either the duty cycle of the inverter (phase-shift control) and having the dc-link voltage fixed, or by changing the dc-link voltage (input dc/dc converter control) and having the duty cycle fixed.

In Fig. 4.11 the output power and efficiency are plotted as a function of phase-shift for a fixed dc-link voltage of 347 V.
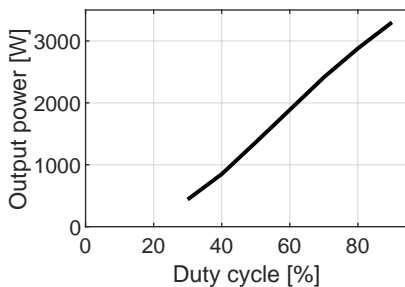
(a) Output power at different duty cycles
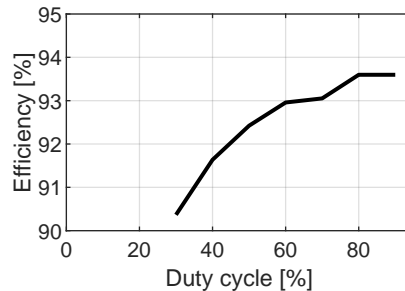
(b) Efficiency at different duty cycles

Figure 4.11: The output power (a) and efficiency (b) with phase-shift control and a dc-link voltage of 347 V

Adding an extra dc/dc converter on the input of the inverter allows for an extra degree of freedom regarding voltage control but adds extra complexity and losses. In Fig. 4.12b the output power is plotted with respect to the input voltage when the duty cycle is fixed at 0.9. Controlling the dc-link voltage is essentially

(a) Output power with different voltages (b) Efficiency with different voltages
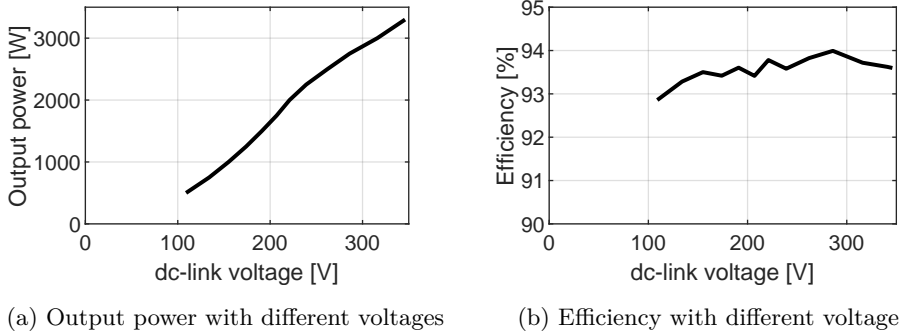
Figure 4.12: Ouput power (a) and efficiency (b) with dc-link voltage control. The duty cycle is fixed at 0.9.

the same as the phase-shift control. However, by having a high duty cycle for the complete operating range the ZVS condition from (4.4) is easier to fulfill since V_{dc} is lower. This can be observed by comparing the efficiencies in Fig. 4.11b and Fig. 4.12b.

If the dc/dc converter is assumed to have an efficiency of 99 % (reported in [46]), the efficiency over the operating range becomes as in Fig. 4.13. If the system is expected to operate at partial load most of the time, it can be beneficial to use an additional dc/dc converter for control. In this case however, charging is mostly done at rated load and the phase-shift control is preferred.
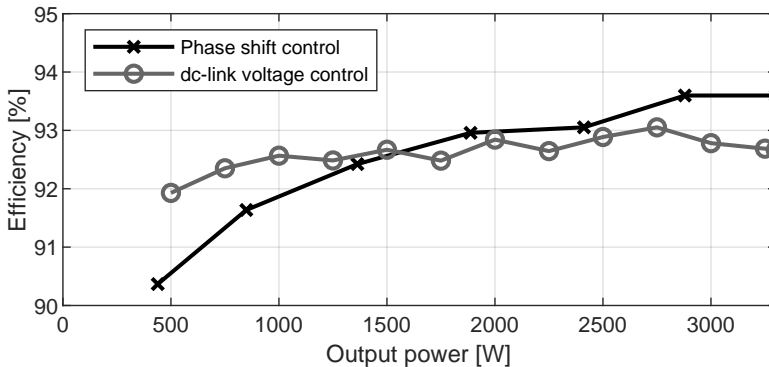
Figure 4.13: Efficiency comparison of phase-shift and dc-link voltage control with 99 % efficiency dc/dc converter.

4.4.2 Stray Field Measurements

With the the charger mounted on the PHEV the magnetic fields are also measured at different points around and inside a vehicle. In Fig. 4.14 the location of the VA and GA and the measurement points are illustrated. At the points around the vehicle (front, rear, left, right) measurements are taken at three heights; 500 mm, 1000 mm and 1500 mm which represents legs, body and head respectively. The magnetic field is measured with the exposure level tester Narda ELT 400 [47].
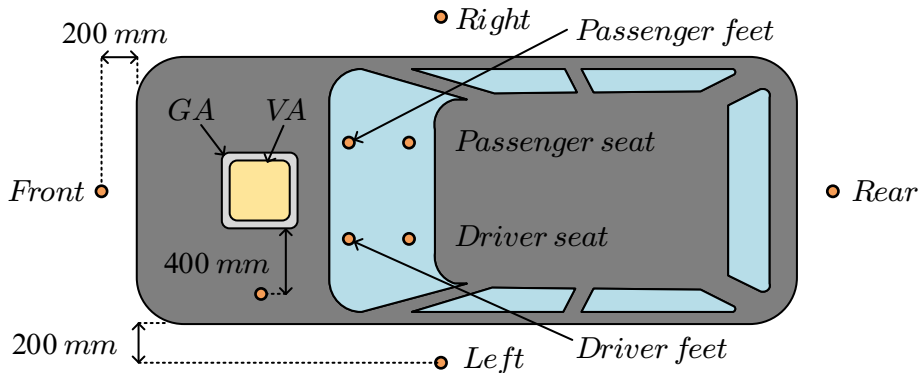
Figure 4.14: Magnetic flux density measurement points inside and around the PHEV test vehicle

For the locations that are considered publicly accessible, the maximum measured magnetic flux density is in front of the vehicle where the measured flux density is 0.24 μT. This is less than 1 % of the allowed limit. If the VA is misaligned by 100 mm the flux density is increased in the front of the vehicle by 62.5 % to 0.39 μT which is 1.5 % of the allowed flux density.

Overall, the stray fields are over-estimated for the simulations compared with the measurements. The largest discrepancy is for the feet on the passenger side where the simulated flux density is more than four times higher than the measured flux density.

Table 4.4: Comparison of measured and simulated magnetic flux density at 3.3 kW

Measurement point		Aligned	GA offset 100 mm to left	FEA (aligned coils)
Left	500 mm	0.08 μT	0.13 μT	0.12 μT
	1000 mm	0.07 μT	0.10 μT	-
	1500 mm	0.06 μT	0.08 μT	-
Right	500 mm	0.10 μT	0.11 μT	0.12 μT
	1000 mm	0.07 μT	0.09 μT	-
	1500 mm	0.06 μT	0.07 μT	-
Front	500 mm	0.24 μT	0.39 μT	0.35 μT
	1000 mm	0.14 μT	0.18 μT	-
	1500 mm	0.08 μT	0.11 μT	-
Rear	500 mm	<0.05 μT	<0.05 μT	-
	1000 mm	<0.05 μT	<0.05 μT	-
	1500 mm	<0.05 μT	<0.05 μT	-
Driver seat	Feet	0.12 μT	0.07 μT	0.22 μT
	Hip	0.06 μT	<0.05 μT	-
	Head	<0.05 μT	<0.05 μT	-
Passenger seat	Feet	<0.05 μT	<0.05 μT	0.22 μT
	Hip	<0.05 μT	<0.05 μT	-
	Head	<0.05 μT	<0.05 μT	-
Under vehicle	400 mm from GA	2.75 μT	-	5.96 μT
	Left front tire	0.69 μT	1.67 μT	1.22 μT

4.5   Summary

In this chapter the design, simulation and experiments of a 3.7 kW IPT charger is presented. The design approach for the secondary coil is based on an optimal loading condition, which is assumed to be when the battery voltage is 300 V. It is shown both with simulations and measurements that a high efficiency is obtained throughout the whole operating range. The size of the coils is based on the analysis presented in Chapter 2, where the primary coil is slightly larger than the secondary coil in order to maximize the coupling factor.

A constant primary side current control is developed. Two methods of achieving this is proposed; either by changing the duty cycle of the inverter and having a fixed dc-link voltage or by having a dc/dc converter and keeping the duty cycle fixed. It is shown that the efficiency at low loads is higher with the dc-link voltage control while for higher loads the phase-shift control is favored.

The VA is mounted on a PHEV and the functionality is proven in a realistic environment. Measurements are done at rated operation in both aligned and 100 mm misaligned conditions. The magnetic field inside and around the PHEV is simulated with FEM. Overall the simulation results agree well with the measurements. It is also verified with the measurements that the stray field is well below the limitations.

5. Fast Charging System

The fast charging system is targeted for 50 kW with a nominal air gap of 180 mm. Two identical full bridge inverters and coils with series-series compensation are built according to the specification in Tab. 5.1. The coil design is based on the work presented in [21] with modifications made in litz wire, cooling and insulation. Additional to the higher efficiency in the rectification the dual-active bridge also allows for bi-directional power flow. A phase-shift between the two inverters can be introduced as an extra control parameter. However, in the tests only passive rectification is utilized through the body diode of the MOSFETs i.e. only the primary inverter is switching for each operating point.

5.1 Simulation Results

A FE model of the coils is done and the self-inductances, coupling factor and magnetic flux densities along the x- and y-direction are obtained. In Fig. 5.1 an illustration of the FE model is shown. The layout of the ferrite bars is done to align the field in the traveling direction (x-direction) and also to fit fans for cooling the coil windings. Two sheets of copper are also added as shielding for the compensation capacitors.

The flux densities in the x- and y-direction are plotted in Fig. 5.2. Comparing the result with the center level result in Fig. 4.7 from the smaller system shows that the field emissions from the systems are similar. Considering that the coils of the 50 kW system are larger, the distance from the coils to the safety limit is equal for the two systems. The simulation results of the coils are presented in Tab. 5.2.

Table 5.1: System specifications and inverter ratings

System specifications			
Input power	52.5 kW	Output power	50 kW
Efficiency	>95 %	Coil sizes	740 mm×450 mm
Air gap	180 mm	Coupling factor	0.15
Inverter ratings			
SiC MOSFET module		Maximum voltage	1200 V
CAS300M12BM2		Maximum current	300 A
		$R_{ds,on}$ @ 25 °C	4.2 mΩ
		Maximum junction temperature	150 °C
		Stray inductance	15 nH
Gate driver		Gate voltage	+20/-6 V
PT62SCMD		Peak output current	±20 A
		Turn on rise time	400 ns
		Turn off fall time	250 ns

Table 5.2: Parameters from FE simulation

Parameter	Value	Parameter	Value
Primary self-inductance	73 μH	Primary series resistance	15.8 mΩ
Secondary self-inductance	73 μH	Secondary series resistance	15.8 mΩ
Coupling factor	0.2		
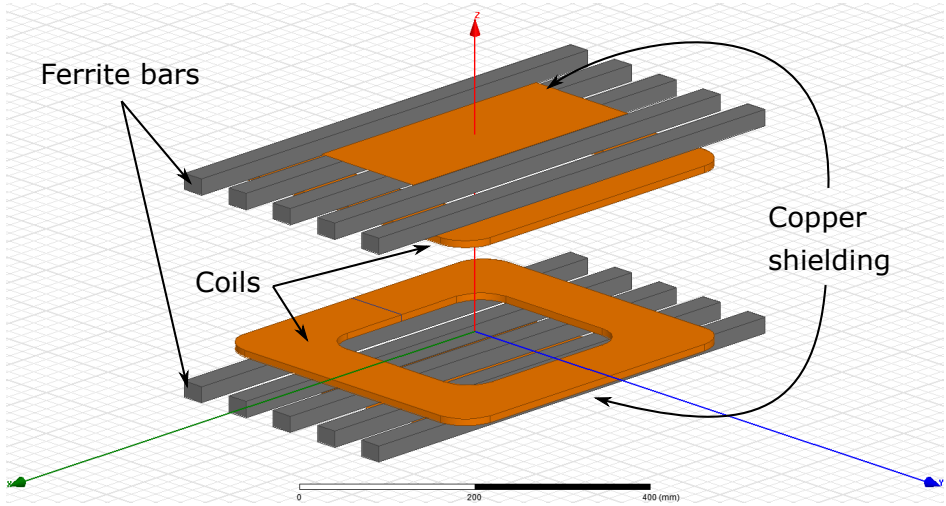
Figure 5.1: FE model of the 50 kW coils

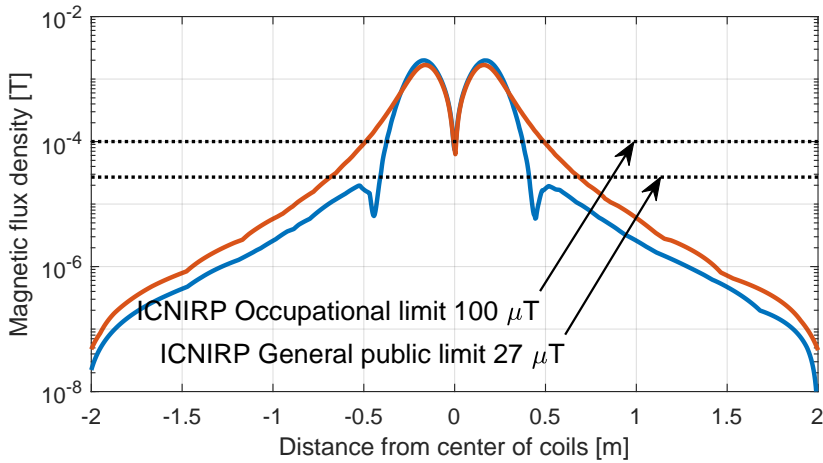Figure 5.2: Flux density along the x-axis (direction of ferrite) and y-axis (perpendicular of ferrite bars) for the coils with rated current.

5.2 Measurement Setups

Tests are performed with two different setups. For the first setup the output is connected to a resistive load to allow for different voltages on the primary and secondary dc-link. The second setup is connected in a back-to-back arrangement,

where the primary and secondary dc-links are connected together and supplied by a power supply.

5.2.1 Generator Supply with Resistive Load

In the first setup the dc-link on the primary side is supplied by a dc generator. Two different generators are available. One is rated for maximum 440 V and 164 A (OL2), and the other is rated for 690 V and 60 A (OL3). The connected load is a 3-phase power resistor with adjustable resistance in discrete steps from 1.2 Ω up to 3.1 Ω. Here, the 3 phases of the power resistor is connected in series, which gives an available load resistance in the range 3.6 Ω to 8.7 Ω. A schematic of the setup is shown in Fig. 5.3.
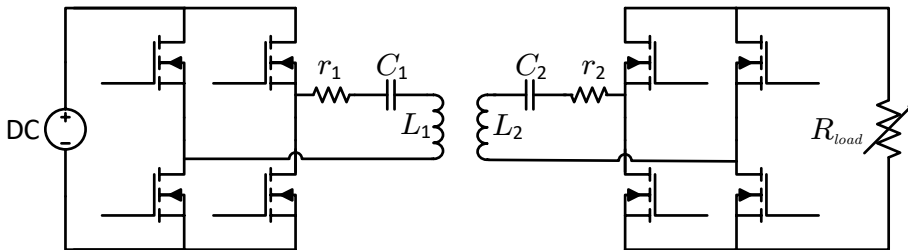
Figure 5.3: Schematic of the setup with a load resistance

5.2.2 Back-to-Back Connection

The second setup is connected in a back-to-back arrangement in order to achieve 50 kW transferred power. A power supply is connected to the dc-links with blocking diodes to protect the power supply from reverse current. In this setup the power supply only has to supply the losses of the system hence a 1000 V/10 A power supply is sufficient. By only measuring the voltage and current from the power supply the losses can be determined. A schematic of the setup is illustrated in Fig. 5.4.
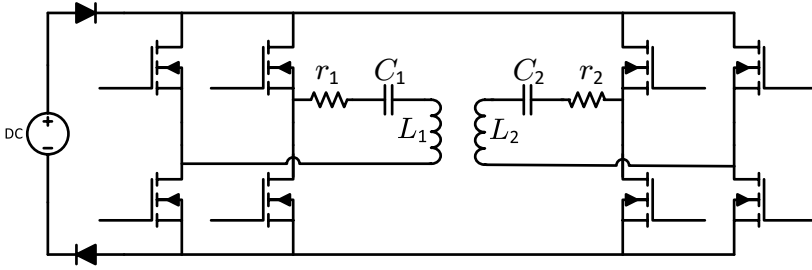
Figure 5.4: Schematic of the back-to-back setup with the DC-links interconnected to the power supply

5.3 Experimental Verification

In Tab. 5.3 the ratings of the materials and components are summarized. A photo of the designed coils and one inverter is shown in Fig. 5.5.
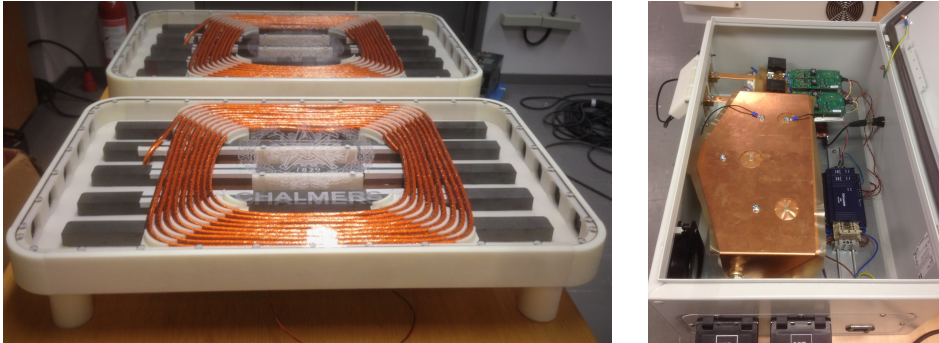
(a) Primary and secondary coil

(b) Full-bridge inverter

Figure 5.5: Coils (a) and inverter (b) for the 50 kW, fast-charging IPT system

Firstly, tests are made with the input dc-link connected to the OL3 generator and the resistive load set to, $R_{load} = 8.7$ Ω. The load is adjusted so that the primary and secondary side currents are equal. In Fig. 5.6 the measured waveforms of the voltages and currents are shown. The efficiency at this operating point is 92.0 % and the maximum efficiency is 94.8 % at 20 kW. A plot of the primary and secondary voltage and current waveforms with 90 kHz switching frequency and 90 % duty cycle is shown in Fig. 5.7. The setup is with the back-to-back arrangement and the dc-link voltage is 650 V. The system efficiency for different power levels is

Table 5.3: Properties and ratings of materials and components of fast charger

Capacitors	Capacitance	330 nF $\pm$ 10%
CSP120/200	Voltage	700 V (RMS)
	Maximum current (f = 85 kHz)	100 A
	Unit layout (series $\times$ parallel)	7 $\times$ 1
	Total capacitance	47.14 nF
	Reactive power	200 kVAr
Litz wire	Number of turns	9.5
Polysol 155	Strand diameter	0.071 mm
	Number of strands	6500
	Maximum temperature	155 °C
Ferrite	Unit layout	5 x 5
I-core 126/20, K2004	Relative permeability	$\mu_r = 2000$
	Loss density (200 mT, 50 kHz)	300 mW/cm^3
Frame	Maximum temperature	140 °C
Nylon 6		
Cover	Maximum temperature	120 °C
Polycarbonate		

Figure 5.6: Measured voltage and current waveforms of the fast charger at 30 kW output power. Primary voltage and current (top), secondary voltage and current (bottom). The duty cycle of the inverter is 90 % and the dc-link voltage from the generator is 650 V.
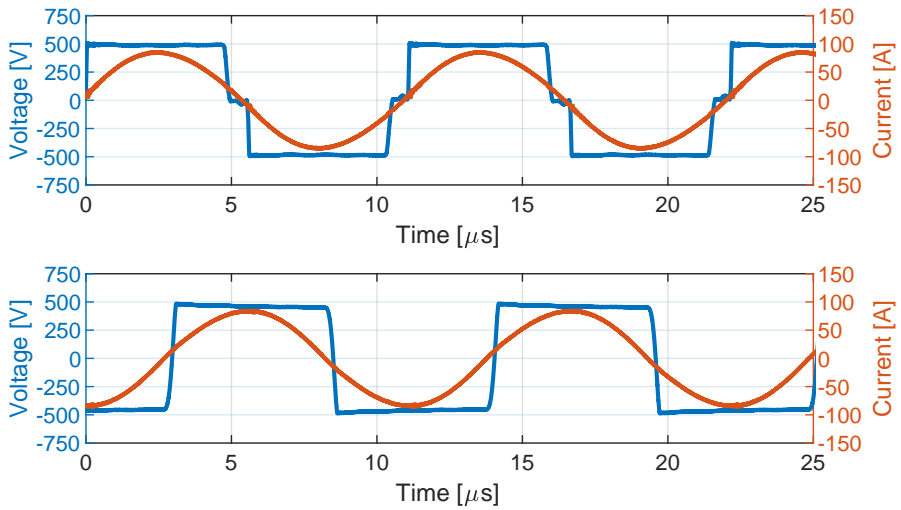
plotted in Fig. 5.8.
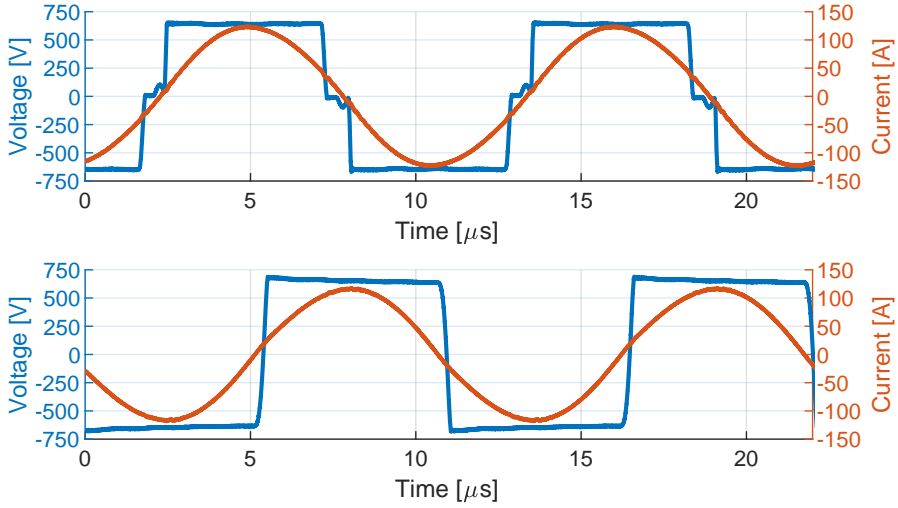
Figure 5.7: Measured voltage and current waveforms of the fast charger at 50 kW output power. Primary voltage and current (top), secondary voltage and current (bottom). The duty cycle is 90 % and the dc-link voltage of the power supply is 650 V.
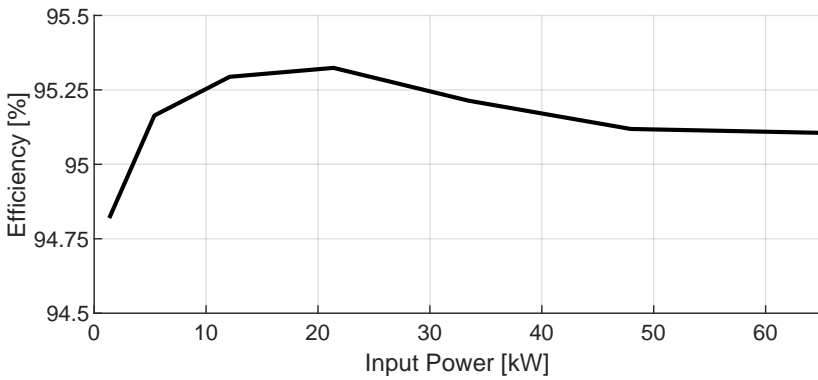
Figure 5.8: Efficiency for different input power

5.4   Summary

High power IPT is a promising solution in applications such as opportunity charging. The functionality and performance of a 50 kW inductive power transfer system is presented in this chapter. Two different system setups are demonstrated. Firstly, a dc generator is used as supply and a power resistor is connected as load. With this setup a maximum of 30 kW power transfer is achievable and the maximum efficiency is 94.8 %. A second setup is tested with a back-to-back arrangement. With the back-to-back setup, power transfer up to 68 kW is tested and the maximum efficiency is 95.3 %. The measurements also show that the dc-dc efficiency is above 95 % for power levels above 10 % of rated power.

The magnetic field distribution is simulated and compared with the simulation results from the 3.3 kW charger. Although the power levels are significantly different, the flux density distributions along the center of the air gaps are similar.

CHAPTER 5.

6. Conclusions and future work

In this thesis, the main principles, the possibilities and the challenges with IPT for EV charging is presented. The design procedure and results for two IPT chargers rated for 3.3 kW and 50 kW output power respectively, are presented. With each chapter containing a summary at the end, only the main conclusions are included here followed by proposals for future work.

6.1 Conclusions

With new wide band-gap semiconductors such as silicon carbide a higher switching frequency can be used and this allows for smaller coil sizes with the same power rating. This is most beneficial on the vehicle side where size is more limited. Decreasing the coil sizes also reduces the amount of material used which reduces the cost of the system.

Furthermore, high efficiency systems ($> 95\%$) are achievable for both low and high power IPT systems. It is evaluated in the analysis that high coupling and quality factors is crucial for high efficiency. This leads to similar sized coils for low and high power transfer with same transfer efficiency and air gaps. The self-inductances of the transmitting and receiving coils are simulated with FEM and an analytical formula is used to estimate the series ac resistances of the coils. The simulated and measured values agrees well.

For the control a method of constant primary side current is proposed. This method utilizes the current capability of the primary side fully, regardless of coupling. In the thesis, constant primary current is realized by either changing the duty cycle or dc-link voltage. With duty cycle control no additional converter

is needed and the control can be implemented by measuring only the primary side current.

The stray fields from an IPT charger are simulated and compared with measurements. In the simulations the vehicle is modeled as a steel sheet that shields the magnetic field. Overall, the simulations and measurements agree well. The biggest discrepancies are observed inside the vehicle where the simulations over-estimates the magnetic flux density. It is concluded that for this setup the limitations on stray fields are fulfilled with ease.

Finally, a high power setup with the primary and secondary side dc-links interconnected is tested. With this back-to-back connection only the losses needs to be supplied and tests with more than 60 kW of transferred power are achieved. With this setup it is also easier and more accurate to measure efficiency since only one voltage measurement and two current measurements are needed. With identical coils the current in each side is approximately equal, meaning that the operation is in the bifurcation-free region and close to the optimal load.

6.2 Future Work

For applications such as opportunity charging and fast charging stations, a high power is desired since the charging time is short. In order to increase the power transfer either the size, the VA rating or the operating frequency can be increased. For the continuation of this project a 200 kW IPT charger is planned. Topics that will be further analyzed are listed as follows:

- Instead of increasing the sizes of the coils, a modular approach can be employed. Several smaller units in parallel which are supplied from separate inverters can be used. Potential benefits with modular units are the possibility of stray field cancellation, flexibility of mounting and that the system can be operated even if one or several units breaks down, although with reduced power.

- A large receiving coil is of concern when it comes to available space on the vehicle. Furthermore, with large coils the distance to accessible area is shorter and stray fields might become a limiting factor. In spite of decreasing the efficiency, a higher power density is essential for high power IPT. Passive or fan cooled coils might not be sufficient to increase the power density, instead liquid cooling can enable higher power density. Except for the better

thermal properties, liquid cooling also improves the breakdown strength and allows for smaller space between turns.

- The work presented in this thesis has focused on coils with passive shielding. It is shown that stray fields are well below the limits for lower power levels. However, for high power levels stray fields may become an important topic that limits the upper boundary of what power levels that are achievable. With active shielding the stray fields can be reduced more effectively.

- Compactness both in terms of space and weight is vital for the success of IPT in EV charging. With wide band-gap materials such as SiC and GaN, the switching frequency of MOSFETs can be increased even further. In the upcoming standard the proposed frequency band is 81.39 - 90 kHz. With higher frequency the amount of magnetic material and coil radii can be smaller, decreasing both the cost and space requirement for the coils.

CHAPTER 6.

References

[1] Legal Information Institute. § 80.22 Controls and prohibitions. [Online]. Available: `https://www.law.cornell.edu/cfr/text/40/80.22` [Accessed: Feb. 19, 2019].

[2] The Engineering Toolbox. [Online]. Available: `https://www.engineeringtoolbox.com/fossil-fuels-energy-content-d_1298.html` [Accessed: Feb. 19, 2019].

[3] ABB. ABB powers e-mobility with launch of first 350 kW high power car charger, 2018. [Online]. Available: `https://new.abb.com/news/detail/4439/abb-powers-e-mobility-with-launch-of-first-350-kw-high-power-car-charger` [Accessed: Feb. 19, 2019].

[4] S. Habibi, F. Sprei, C. Englund, S. Pettersson, A. Voronov, J. Wedin, and H. Engdahl. Comparison of free-floating car sharing services in cities. *ECEEE Summer Study*, May-June 2017.

[5] E. Arfa Grunditz and T. Thiringer. Characterizing BEV Powertrain Energy Consumption, Efficiency, and Range During Official and Drive Cycles From Gothenburg, Sweden. *IEEE Transactions on Vehicular Technology*, 65(6):3964–3980, June 2016.

[6] Saurin Sheth, Kavit H. Patel, and Harsh Patel. Design of automatic fuel filling system using a mechatronics approach. In Dipak Kumar Mandal and Chanan Singh Syan, editors, *CAD/CAM, Robotics and Factories of the Future*, pages 785–795, New Delhi, 2016. Springer India.

[7] E. Palermo. Tesla Unveils Snakelike Robot Charger for Electric Cars. Live Science, 2015. [Online]. Available: `https://www.livescience.com/51791-tesla-electric-car-robot-charger.html` [Accessed: Feb. 19, 2019].

[8] Volvo Bus Corporation. Volvo opportunity charging system. [Online]. Available: `https://www.volvobuses.se/content/dam/volvo/volvo-buses/master/bre/our-offering/documents/FactsheetOpportunityChargingSystemEN2015_00733.pdf` [Accessed: Feb. 19, 2019].

[9] Siemens. eHighway - Electrification of road freight transport. [Online]. Available: `https://new.siemens.com/global/en/products/mobility/road-solutions/electromobility/ehighway.html` [Accessed: Feb. 19, 2019].

[10] P. Abrahamsson and M. Alaküla. Thermal modeling of an ERS during static charging. In *2018 IEEE International Conference on Electrical Systems for Aircraft, Railway, Ship Propulsion and Road Vehicles International Transportation Electrification Conference (ESARS-ITEC)*, pages 1–6, Nov 2018.

[11] H. Sakamoto, K. Harada, S. Washimiya, K. Takehara, Y. Matsuo, and F. Nakao. Large air-gap coupler for inductive charger [for electric vehicles]. *IEEE Transactions on Magnetics*, 35(5):3526–3528, Sep. 1999.

[12] S. Valtchev, B. Borges, K. Brandisky, and J. B. Klaassens. Resonant Contactless Energy Transfer With Improved Efficiency. *IEEE Transactions on Power Electronics*, 24(3):685–699, March 2009.

[13] J. Huh, S. W. Lee, W. Y. Lee, G. H. Cho, and C. T. Rim. Narrow-Width Inductive Power Transfer System for Online Electrical Vehicles. *IEEE Transactions on Power Electronics*, 26(12):3666–3679, Dec 2011.

[14] M. Budhia, G. A. Covic, J. T. Boys, and C. Huang. Development and evaluation of single sided flux couplers for contactless electric vehicle charging. In *2011 IEEE Energy Conversion Congress and Exposition*, pages 614–621, Sep. 2011.

[15] S. Bandyopadhyay, P. Venugopal, J. Dong, and P. Bauer. Comparison of Magnetic Couplers for IPT based EV Charging using Multi-Objective Optimization. *IEEE Transactions on Vehicular Technology*, pages 1–1, 2019.

[16] F. Y. Lin, G. A. Covic, and J. T. Boys. Evaluation of Magnetic Pad Sizes and Topologies for Electric Vehicle Charging. *IEEE Transactions on Power Electronics*, 30(11):6391–6407, Nov 2015.

[17] R. Bosshard, U. Iruretagoyena, and J. W. Kolar. Comprehensive Evaluation of Rectangular and Double-D Coil Geometry for 50 kW/85 kHz IPT System. *IEEE Journal of Emerging and Selected Topics in Power Electronics*, 4(4):1406–1415, Dec 2016.

[18] WiTricity. [Online]. Available: `http://witricity.com/products/automotive/` [Accessed: Feb. 19, 2019].

[19] V. P. Galigekere, J. Pries, O. C. Onar, G. Su, S. Anwar, R. Wiles, L. Seiber, and J. Wilkins. Design and Implementation of an Optimized 100 kW Stationary Wireless Charging System for EV Battery Recharging. In *2018 IEEE Energy Conversion Congress and Exposition (ECCE)*, pages 3587–3592, Sep. 2018.

[20] J. Shin, S. Shin, Y. Kim, S. Ahn, S. Lee, G. Jung, S. Jeon, and D. Cho. Design and Implementation of Shaped Magnetic-Resonance-Based Wireless Power Transfer System for Roadway-Powered Moving Electric Vehicles. *IEEE Transactions on Industrial Electronics*, 61(3):1179–1192, March 2014.

[21] R. Bosshard and J. W. Kolar. Multi-Objective Optimization of 50 kW/85 kHz IPT System for Public Transport. *IEEE Journal of Emerging and Selected Topics in Power Electronics*, 4(4):1370–1382, Dec 2016.

[22] A. Tejeda, S. Kim, F. Y. Lin, G. A. Covic, and J. T. Boys. A Hybrid Solenoid Coupler for EV Wireless Charging Applications. *IEEE Transactions on Power Electronics*, pages 1–1, 2018.

[23] Plugless. [Online]. Available: `https://www.pluglesspower.com/` [Accessed: Feb. 19, 2019].

[24] Wireless Power Transfer for Light-Duty Plug-In/ Electric Vehicles and Alignment Methodology, May 2016. SAE TIR J2954.

[25] ICNIRP guidelines for limiting exposure to time-varying electric and magnetic fields (1 Hz – 100 kHz), 2010. Published in: HEALTH PHYSICS 99(6):818-836; 2010.

[26] A. Ghahary and B. H. Cho. Design of transcutaneous energy transmission system using a series resonant converter. *IEEE Transactions on Power Electronics*, 7(2):261–269, April 1992.

[27] A. Kawamura, K. Ishioka, and J. Hirai. Wireless transmission of power and information through one high frequency resonant AC link inverter for robot manipulator applications. In *IAS '95. Conference Record of the 1995 IEEE*

Industry Applications Conference Thirtieth IAS Annual Meeting, volume 3, pages 2367–2372 vol.3, Oct 1995.

[28] C. S. Wang, G. A. Covic, and O. H. Stielau. Power transfer capability and bifurcation phenomena of loosely coupled inductive power transfer systems. *IEEE Transactions on Industrial Electronics*, 51(1):148–157, Feb 2004.

[29] S. Chopra and P. Bauer. Analysis and design considerations for a contactless power transfer system. In *2011 IEEE 33rd International Telecommunications Energy Conference (INTELEC)*, pages 1–6, Oct 2011.

[30] W. Zhang and C. C. Mi. Compensation Topologies of High-Power Wireless Power Transfer Systems. *IEEE Transactions on Vehicular Technology*, 65(6):4768–4778, June 2016.

[31] Y. Liu, P. A. Hu, and U. K. Madawala. Maximum power transfer and efficiency analysis of different inductive power transfer tuning topologies. In *2015 IEEE 10th Conference on Industrial Electronics and Applications (ICIEA)*, pages 649–654, June 2015.

[32] C. R. Paul. *The Concept of Loop Inductance*. IEEE, 2010.

[33] W. A. Roshen and D. E. Turcotte. Planar inductors on magnetic substrates. *IEEE Transactions on Magnetics*, 24(6):3213–3216, Nov 1988.

[34] C. R. Sullivan. Optimal choice for number of strands in a litz-wire transformer winding. *IEEE Transactions on Power Electronics*, 14(2):283–291, March 1999.

[35] Ferroxcube. Dataset on Steinmetz coefficients. [Online]. Available: `https://www.ferroxcube.com/upload/media/design/FXCStainmetzCoefficients.xls` [Accessed: Apr. 26, 2019].

[36] W. Zhang, S. Wong, C. K. Tse, and Q. Chen. Analysis and Comparison of Secondary Series- and Parallel-Compensated Inductive Power Transfer Systems Operating for Optimal Efficiency and Load-Independent Voltage-Transfer Ratio. *IEEE Transactions on Power Electronics*, 29(6):2979–2990, June 2014.

[37] T. Campi, S. Cruciani, F. Maradei, and M. Feliziani. Near-Field Reduction in a Wireless Power Transfer System Using LCC Compensation. *IEEE Transactions on Electromagnetic Compatibility*, 59(2):686–694, April 2017.

[38] S. Li, W. Li, J. Deng, T. D. Nguyen, and C. C. Mi. A Double-Sided LCC Compensation Network and Its Tuning Method for Wireless Power Transfer. *IEEE Transactions on Vehicular Technology*, 64(6):2261–2273, June 2015.

[39] A. Safaee and K. Woronowicz. Time-Domain Analysis of Voltage-Driven Series–Series Compensated Inductive Power Transfer Topology. *IEEE Transactions on Power Electronics*, 32(7):4981–5003, July 2017.

[40] R. L. Steigerwald. A comparison of half-bridge resonant converter topologies. *IEEE Transactions on Power Electronics*, 3(2):174–182, April 1988.

[41] S. Skoog. Parameterization of equivalent circuit models for high power lithium-ion batteries in HEV applications. In *2016 18th European Conference on Power Electronics and Applications (EPE'16 ECCE Europe)*, pages 1–10, Sep. 2016.

[42] G. A. Covic and J. T. Boys. Inductive Power Transfer. *Proceedings of the IEEE*, 101(6):1276–1289, June 2013.

[43] K. Aditya and S. S. Williamson. Design Guidelines to Avoid Bifurcation in a Series–Series Compensated Inductive Power Transfer System. *IEEE Transactions on Industrial Electronics*, 66(5):3973–3982, May 2019.

[44] W. Niu, J. Chu, W. Gu, and A. Shen. Exact Analysis of Frequency Splitting Phenomena of Contactless Power Transfer Systems. *IEEE Transactions on Circuits and Systems I: Regular Papers*, 60(6):1670–1677, June 2013.

[45] Texas Instruments. *Phase-Shifted Full-Bridge, Zero-Voltage Transition Design Considerations*, 2011. Application Report.

[46] R. Bosshard and J. W. Kolar. All-SiC 9.5 kW/dm3 On-Board Power Electronics for 50 kW/85 kHz Automotive IPT System. *IEEE Journal of Emerging and Selected Topics in Power Electronics*, 5(1):419–431, March 2017.

[47] NARDA. Exposure level tester. [Online]. Available: `https://www.narda-sts.com/en/emc-products/elt-400/` [Accessed: Feb. 25, 2019].

APPENDIX .

Appendix A.
Magnetic flux density from a coil in free space

In order to calculate the magnetic flux density, a vector field called magnetic vector potential, denoted $\vec{A}$, is introduced. The magnetic vector potential is defined as

$$\vec{B} = \nabla \times \vec{A}. \tag{A.1}$$

Assume a point P located at $(\vec{x}) = (x_P, y_P, z_P)$, and a current loop centered around the origin with radius a and current I. The cartesian coordinates for the current loop is defined as $(\vec{x}') = (x_I, y_I, z_I)$ where $a = \sqrt{(x_I^2 + y_I^2)}$ and $z_I = 0$. An illustration of the current loop and the point P is shown in Fig. A.1.

The vector potential can then be calculated as

$$\vec{A}(\vec{x}) = \frac{\mu_0}{4\pi} \int \frac{\vec{J}(\vec{x}')}{|\vec{x} - \vec{x}'|} \, \mathrm{d}^3 \vec{x}' \tag{A.2}$$

where $\vec{J}(\vec{x}')\mathrm{d}^3\vec{x}'$ can be re-written as

$$\vec{J}(\vec{x}') \, \mathrm{d}^3 \vec{x}' = I \, \mathrm{d}\vec{x}'. \tag{A.3}$$

Due to symmetry, the point P can be chosen arbitrary with respect to ϕ in spherical coordinates and it is convenient to chose P such as $\phi_P = \pi/2$. The point

APPENDIX A.
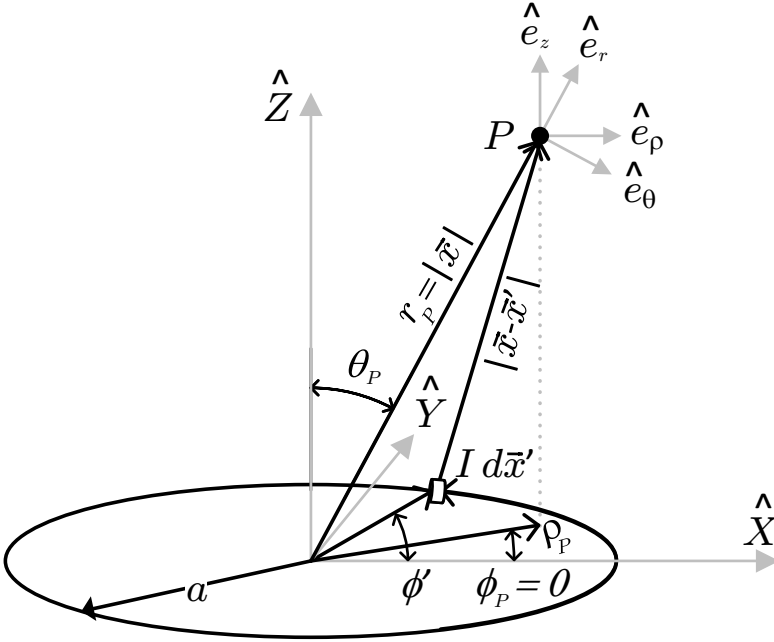

Figure A.1: Coordinate system for current loop and a point P

P in cartesian coordinates can be expressed in spherical coordinates as:

$$x_P = r_P \cdot \sin(\theta_P) \cdot \overbrace{\cos(\phi_P)}^{=0} \qquad y_P = r_P \cdot \sin\theta_P \cdot \overbrace{\sin(\phi_P)}^{=0} \qquad z_P = r_P \cdot \cos(\theta_P)$$
$$\underbrace{}_{=1}$$

$$\boxed{x_P = r_P \cdot \sin(\theta_P)} \qquad\qquad \boxed{y_P = 0} \qquad\qquad\qquad \boxed{z_P = r_P \cdot \cos(\theta_P)}$$

$$x_I = a \cdot \underbrace{\overbrace{\sin(\theta')}^{=\pi/2}}_{=1} \cdot \cos(\phi') \qquad y_I = a \cdot \underbrace{\overbrace{\sin(\theta')}^{=\pi/2}}_{=1} \cdot \sin(\phi') \qquad z_I = r \cdot \underbrace{\overbrace{\cos(\theta')}^{=\pi/2}}_{=0}$$

$$\boxed{x_I = a \cdot \cos(\phi')} \qquad\qquad \boxed{y_I = a \cdot \sin(\phi')} \qquad\qquad \boxed{z_I = 0}$$

$$(A.4)$$

The current loop along $\vec{x}'$ can then be expressed as

$$
\begin{aligned}
\vec{x}'(\phi') &= a \cdot \cos \phi' \hat{e}_x + a \cdot \sin \phi' \hat{e}_y \\
d\vec{x}' &= (-a \cdot \sin \phi' \hat{e}_x + a \cdot \cos \phi' \hat{e}_y) d\phi' \\
&= (-\sin \phi' \hat{e}_x + \cos \phi' \hat{e}_y) a d\phi' \\
\phi' &= [0, 2\pi]
\end{aligned}
\tag{A.5}
$$

where $\hat{e}_x$ and $\hat{e}_y$ are the unit vectors in x and y direction respectively and ϕ' is the angle in the xy-plane from the x-axis to the current element $I \, d\vec{\phi'}$. This gives the magnetic vector potential at point P,

$$
\begin{aligned}
\vec{A}(\vec{x}) &= \frac{\mu_0 I}{4\pi} \int_0^{2\pi} \frac{dx_I}{|\vec{x} - \vec{x}'|} = \frac{\mu_0 I a}{4\pi} \int_0^{2\pi} \frac{(-\sin(\phi')\hat{e}_x + \cos(\phi')\hat{e}_y) \, d\phi'}{|\vec{x} - \vec{x}'|} = \\
&= \frac{\mu_0 I a}{4\pi} \left(\underbrace{\int_0^{2\pi} \frac{(-\sin(\phi')\hat{e}_x)}{|\vec{x} - \vec{x}'|} d\phi'}_{=0} + \int_0^{2\pi} \frac{(\cos(\phi')\hat{e}_y)}{|\vec{x} - \vec{x}'|} d\phi' \right) = \\
&= \frac{\mu_0 I a}{4\pi} \int_0^{2\pi} \frac{\cos(\phi')\hat{e}_y}{|\vec{x} - \vec{x}'|} d\phi'.
\end{aligned}
\tag{A.6}
$$

The x-part becomes zero due to the sinus part, thus the vector potential will only be directed in the $\hat{e}_y$ direction. The distance $|\vec{x} - \vec{x}'| = \sqrt{(x_P - x_I)^2 + (y_P - y_I)^2 + (z_P - z_I)^2}$ with the values from (A.4) gives

$$
|\vec{x} - \vec{x}'| = \sqrt{r_P^2 + a^2 - 2 \cdot r_P \cdot a \cdot \sin(\theta_P) \cdot \cos(\phi')}
\tag{A.7}
$$

Inserting (A.7) into (A.6) results in the magnetic vector potential in spherical coordinates

$$
\vec{A}(\vec{x}) = \frac{\mu_0 I a}{4\pi} \int_0^{2\pi} \frac{\cos(\phi')\hat{e}_\phi}{\sqrt{r_P^2 + a^2 - 2 \cdot r_P \cdot a \cdot \sin(\theta_P) \cdot \cos(\phi')}} d\phi'.
\tag{A.8}
$$

The vector $\vec{A}$ is only directed in y-direction, or equivalently ϕ-direction in spherical coordinates. Equation (A.8) is an elliptical integral and to solve it the identity $\cos(\phi') = 1 - 2\sin(\frac{\phi'}{2})$ is used. Furthermore, the following relations are introduced for visibility:

$$
\begin{aligned}
A_k &= r_P^2 + a^2 \\
B_k &= 2 \cdot r \cdot a \cdot \sin(\theta_P) \\
C_k &= \frac{\mu_0 I a}{4\pi}.
\end{aligned}
$$

Inserting in (A.8) gives the vector potential in ϕ-direction,

APPENDIX A.

$$A_\phi(\vec{x}) = C \int_0^{2\pi} \frac{\cos(\phi')}{\sqrt{A - B \cdot \cos(\phi')}} \, d\phi' = 2C \int_0^\pi \frac{\cos(\phi')}{\sqrt{A - B \cdot \cos(\phi')}} \, d\phi' =$$

$$= 2C \int_0^\pi \frac{1 - 2\sin^2\left(\frac{\phi'}{2}\right)}{\sqrt{A - B(1 - 2\sin^2\left(\frac{\phi'}{2}\right))}} \, d\phi' = [\phi' = 2t \quad d\phi' = 2dt] =$$

$$= 4C \int_0^{t=\pi/2} \frac{1 - 2\sin^2(t)}{\sqrt{A - B(1 - 2\sin^2(t))}} \, dt =$$

$$= 4C \left[\int_0^{\pi/2} \frac{dt}{\sqrt{A - B + 2B \cdot \sin^2(t)}} - \int_0^{\pi/2} \frac{2\sin^2(t)}{\sqrt{A - B + 2B \cdot \sin^2(t)}} \, dt \right] =$$

$$= \frac{4C}{\sqrt{A-B}} \left[\underbrace{\int_0^{\pi/2} \frac{dt}{\sqrt{1 - \left(\frac{2B}{B-A}\right) \cdot \sin^2(t)}}}_{F(k_B^2)} - \underbrace{\int_0^{\pi/2} \frac{2\sin^2(t)}{\sqrt{1 - \left(\frac{2B}{B-A}\right) \cdot \sin^2(t)}} \, dt}_{2D(k_B^2)} \right]$$

$$\text{(A.9)}$$

where $D(k_B^2) = \frac{F(k_B^2) - E(k_B^2)}{k_B^2}$ and $F(k_B^2)$ and $E(k_B^2)$ are the complete elliptical integrals of first and second kind respectively, defined as

$$F(k_B^2) = \int_0^{\pi/2} \frac{d\phi'}{\sqrt{1 - k_B^2 \cdot \sin^2 \phi'}}$$

$$E(k_B^2) = \int_0^{\pi/2} \sqrt{1 - k_B^2 \cdot \sin^2 \phi'} \, d\phi' \tag{A.10}$$

and k_B^2 is the elliptical modulus

$$k_B^2 = \frac{2B}{B - A}. \tag{A.11}$$

The magnetic vector potential in ϕ-direction can now be written in terms of the elliptical integrals, $F(k_B^2)$ and $E(k_B^2)$, as

$$A_\phi(\vec{x}) = \frac{4C}{\sqrt{A-B}}[F(k_B^2) - 2D(k_B^2)] =$$

$$= \frac{4C}{\sqrt{A-B}} \left[\frac{2B \cdot F(k_B^2) - 2(B-A) \cdot (F(k_B^2) - E(k_B^2))}{2B} \right] =$$

$$\boxed{A_\phi(\vec{x}) = \frac{4C}{B\sqrt{(A-B)}}[AF(k_B^2) + (B-A)E(k_B^2)].} \tag{A.12}$$

It can been noted that the magnetic vector potential only has a ϕ-component. From the definition of the magnetic vector potential (A.1), the magnetic flux

density can now be written in spherical coordinates

$$\vec{B}(\vec{x}) = \nabla \times \vec{A}(\vec{x}) = \frac{\partial A_\phi(\vec{x})}{\partial r}\hat{e}_\theta - \frac{\partial A_\phi(\vec{x})}{\partial \theta}\hat{e}_r. \tag{A.13}$$

The part of $\vec{B}$ that induces voltage into the secondary coil is the $\hat{e}_z$ component, hence it is more convenient to express the result in cylindrical coordinates. The parameters; $A_k(r_P)$, $B_k(r_P, \theta_P)$ and $k^2(r_P, \theta_P)$ in $A_\phi(\vec{x} = (r_P, \theta_P, \overbrace{\phi_P}^{=0}))$ transformed into cylindrical coordinates ($\vec{x} = (\rho_P, \phi_P, z_P)$) becomes:

$$\begin{aligned}
r_P^2 &= \rho_P^2 + z_P^2 \\
\rho_P &= r_P \cdot \sin(\theta_P) \\
A_k &= r_P^2 + a^2 = \rho_P^2 + z_P^2 + a^2 \\
B_k &= 2ra \cdot \sin(\theta_P) = 2a\rho_P \\
k_B^2 &= \frac{2B}{B-A} = \frac{4a\rho_P}{2ax_P - (a^2 + \rho_P^2 + z_P^2)}.
\end{aligned} \tag{A.14}$$

It can be noted that ρ_P is the same as x_P in cartesian coordinates, due to that $\phi_P = \pi/2$. The calculation of $\vec{B}(\vec{x})$ in cylindrical coordinates becomes

$$\vec{B}(\vec{x}) = \nabla \times \vec{A}(\vec{x}) = \frac{1}{\rho}\begin{bmatrix} \hat{e}_\rho & \rho\hat{e}_\phi & \hat{e}_z \\ \frac{\partial}{\partial \rho} & \frac{\partial}{\partial \phi} & \frac{\partial}{\partial z} \\ A_\rho & \rho A_\phi & A_z \end{bmatrix}. \tag{A.15}$$

Since $A_\rho = A_z = 0$ the magnetic flux density, $\vec{B}$, is

$$\vec{B}_{\rho z} = \frac{1}{\rho}\frac{\partial(\rho A_\phi)}{\partial \rho}\hat{e}_z - \frac{1}{\rho}\frac{\partial(\rho A_\phi)}{\partial z}\hat{e}_\rho. \tag{A.16}$$

The evaluation of (A.16) is tedious (but straight-forward) and here a symbolic software is used to express $B_\rho(\rho_P, z_P)$ and $B_z(\rho_P, z_P)$, the final expressions becomes

$$\boxed{B_\rho(\rho_P, z_P) = \frac{\mu_0 I z_P}{2\pi\rho_P\sqrt{(a-\rho_P)^2 + z_P^2}}\left(\frac{a^2 + \rho_P^2 + z_P^2}{(a+\rho_P)^2 + z_P^2}E(k_B^2) - F(k_B^2)\right)}$$

$$\boxed{B_z(\rho_P, z_P) = \frac{\mu_0 I z_P}{2\pi\sqrt{(a-\rho_P)^2 + z_P^2}}\left(\frac{a^2 - \rho_P^2 - z_P^2}{(a+\rho_P)^2 + z_P^2}E(k_B^2) + F(k_B^2)\right).}$$

$$\tag{A.17}$$